Analysis of the Effect of the August 2017 Eclipse on the Ionosphere Using a Ray-trace Algorithm

Magdalina Moses

Thesis submitted to the faculty of the Virginia Polytechnic Institute and State University in partial fulfillment of the requirements for the degree of

Master of Science
In
Electrical Engineering

Gregory D. Earle, Chair
J. Michael Ruohoniemi
Dennis Sweeney

July 1, 2019
Blacksburg, Virginia

Keywords: Ionosphere, Eclipses, Ray-trace, SuperDARN, 2017 Eclipse

Analysis of the Effect of the August 2017 Eclipse on the Ionosphere Using a Ray-trace Algorithm

Magdalina Moses

Academic Abstract

The total solar eclipse over the continental United States on August 21, 2017 offered a unique opportunity to study the dependence of the ionospheric density and morphology on incident solar radiation. Unique responses may be witnessed during eclipses, including changes in radio frequency (RF) propagation at high frequency (HF). Such changes in RF propagation were observed by the Super Dual Auroral Radar Network (SuperDARN) radars in Christmas Valley, Oregon and in Fort Hays, Kansas during the 2017 eclipse. At each site, the westward looking radar observed an increase in slant range of the backscattered signal during the eclipse onset followed by a decrease after totality. In order to investigate the underlying processes governing the ionospheric response to the eclipse, we employ the HF propagation toolbox (PHaRLAP), created by Dr. Manuel Cervera, to simulate SuperDARN data for different models of the eclipsed ionosphere. Thus, by invoking different hypotheses and comparing simulated results to SuperDARN measurements, we can study the underlying processes governing the ionosphere and improve our model of the ionospheric responses to an eclipse. This thesis presents three studies using this method: identification of the cause of the increase in slant range observed by SuperDARN during the eclipse; evaluation of different eclipse obscuration models; and quantification of the effect of the neutral wind velocity on the simulated eclipse data.

Analysis of the Effect of the August 2017 Eclipse on the Ionosphere Using a Ray-trace Algorithm

Magdalina Moses

General Audience Abstract

The ionosphere is the charged layer of the upper atmosphere, which is generated and sustained by sunlight ionizing neutral particles to form a plasma. In the absence of sunlight, ions and electrons can recombine into neutral particles. The total solar eclipse over the continental United States on August 21, 2017 offered a unique opportunity to study the dependence of the ionospheric density and plasma motion on sunlight as the period of the eclipse is much shorter than night. Observations of the ionosphere during past eclipses indicate that unique ionospheric behavior may be witnessed during eclipses, including changes in radio wave propagation for radio waves in the high frequency (HF) regime. Such changes in radio propagation were observed by the Super Dual Auroral Radar Network (SuperDARN) ionospheric HF radars in Christmas Valley, Oregon and in Fort Hays, Kansas during the 2017 eclipse. At each site, the westward looking radar observed an increase in distance that the radio waves traveled before they were reflected back to the radar during the eclipse onset followed by a decrease in this distance after totality. In order to investigate the mechanisms that produce these observed effects, we employed the HF propagation toolbox (PHaRLAP), created by Dr. Manuel Cervera, to simulate radio propagation and generate simulated SuperDARN data for different models of the eclipsed ionosphere. Thus, different models can be tested by comparing simulated data to measured data. Hence, we can study the underlying processes governing the ionosphere and improve our model of the ionospheric responses to an eclipse. This thesis presents three studies using this method to: identify the cause of the increase in the distance radio waves traveled during the eclipse; evaluate different models of change in eclipse magnitude over time; and investigate the effect of the neutral wind velocity on the simulated eclipse data.

Table of Contents

List of Abbreviations

BKS: Blackstone [radar]
CONUS: Continental United States
CV: Christmas Valley
CVE: Christmas Valley East [radar]
CVW: Christmas Valley West [radar]
FH: Fort Hays
FHE: Fort Hays East [radar]
FHW: Fort Hays West [radar]
foF2: Ordinary mode critical frequency of the F2 layer
FOV: Field-of-View
HWM: Horizontal-Wind-Model
Hz: Hertz
IGRF: International Geomagnetic Reference Field
IRI: International Reference Ionosphere
ISR: Incoherent Scatter Radar
LT: Local Time
MSIS: [model based on] Mass Spectrometer and Incoherent Scatter data
NRL: Naval Research Laboratory
PHaRLAP: Provision of High-frequency Raytracing Laboratory for Propagation studies [ray-trace toolbox]
RTI: Range-Time-Intensity [plot]
SAMI: Sami Is Another Model Ionosphere
SAMI2: SAMI 2D
SAMI3: SAMI 3D
SNR: Signal-to-Noise Ratio
SSUSI: Special Sensor Ultraviolet Spectrographic Imager
STA: Scatter-Time-Azimuth [plot]
SuperDARN: Super Dual Auroral Radar Network
US: United States
UT: Universal Time
WAL: Wallops [radar]

Chapter 1

1.1 2017 Eclipse

1.1.1 2017 Eclipse Introduction

On August 21, 2017, a total solar eclipse occurred over the continental United States (CONUS). The path of the eclipse over the CONUS stretched from Oregon to South Carolina as shown in Figure 1.

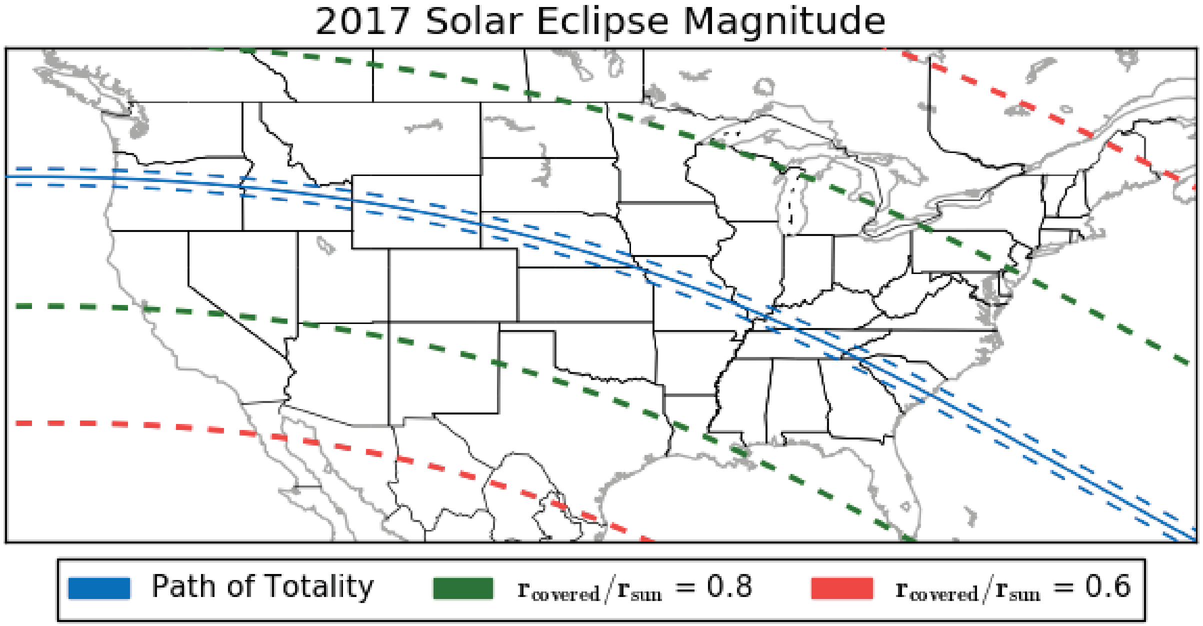

Figure 1. 2017 eclipse path of totality and curves of equal magnitude of the fraction of sun's diameter obscured at maximum eclipse (Data from (Jubier 2005)).

The eclipse started in the Pacific Ocean near 16:00 UT and ended in the Atlantic Ocean around 21:00 UT. The duration of the eclipse along the path of totality from the start of the partial phase to the end of the partial phase varied from about one and a half hours to two hours and fifty-five minutes depending on location. Along the path of totality, the duration of totality ranged from about 47 seconds to about two minutes and 40 seconds. The eclipse magnitude, defined as “the fraction of the diameter of the sun eclipsed by the Moon (Espenak , NASA)”, varies with time and location as shown in Figure 1. The maximum eclipse magnitude was 1.015, which occurred in southern Illinois. The umbra of the eclipse had an average width of about 105 km in the CONUS. The penumbra of the eclipse was much wider than the umbra, reaching a maximum latitude of about 82ºN and a minimum latitude of about 20ºS. Figure 1 illustrates the expanse of the eclipse penumbra across the CONUS.

1.1.2 Previous Eclipse Studies

Since the early-to-mid 1900s, researchers have conducted experiments to observe ionospheric phenomena that arise as effects of an eclipse. However, the ionospheric effects of eclipses vary by magnetic latitude, time of day, and geomagnetic conditions. Even when ionospheric measurements were made during different eclipses under similar conditions, the results are sometimes contradictory. Despite these inconsistencies, some commonly observed effects of eclipses on the ionosphere include a decrease in the ionospheric plasma density and a change in the height of the peak plasma density of some ionospheric layers.

One notable eclipse study was conducted in western Europe during the August 1999 eclipse, using the Chilton ionosonde in Great Britain. A plot of these foF2 data obtained with the Chilton ionosonde during the eclipse is shown in Figure 2; it shows a significant decrease in foF2 at the onset of the eclipse (with maximum eclipse occurring around 10:16 UT at F2 region altitudes). This decrease is a distinct deviation from the value given by the International Reference Ionosphere (IRI) model for that date. Since foF2 is proportional to the square root of the electron density, the measured decrease in foF2 corresponds to a significant decrease in the ionospheric electron density during the eclipse.

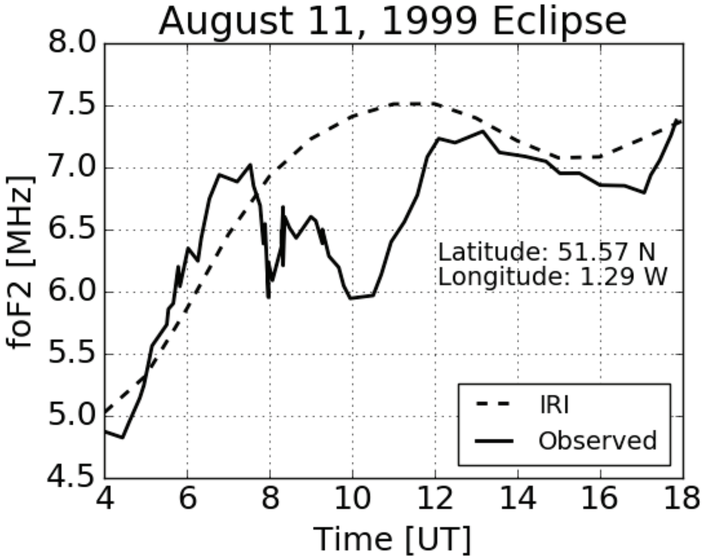

Figure 2. Effect of the August 11, 1999 eclipse on foF2. The decrease in the observed foF2 (solid line) (Afraimovich, Kosogorov et al. 2002) from the IRI model (dashed line) over a long period coincides with partial obscuration of the solar disk.

Results from other eclipses have indicated that there is also a large spatial effect on the ionosphere extending well outside the eclipse's region of totality. For example, the Special Sensor Ultraviolet Spectrographic Imager (SSUSI) instrument observed a depleted airglow region roughly 1,000 km in diameter around the ~ 174km wide eclipse path of totality during the March 29, 2006 solar eclipse over western Africa.

1.1.3 Predicted 2017 Eclipse Effects

The plasma density in the ionosphere is dependent on sunlight, which creates plasma by ionizing neutral atmospheric particles. At night the ionosphere experiences a decrease in plasma density at all altitudes because the electrons and ions recombine to form neutral particles, as shown in Figure 3. When the sun is obscured during the eclipse, the density of the ionosphere will also decrease, especially at low altitudes where the recombination is fast. However, the time scale at which the eclipse blocks most of the sunlight is much shorter than diurnal variations, and the corona remains visible during an eclipse. This suggests that during an eclipse the ionosphere will not experience a decrease in electron density as significant as that which occurs overnight. Since the magnitude of the eclipse varies with latitude (Figure 1), any eclipse-induced decreases in plasma density may vary with eclipse magnitude. If this occurs, then ionospheric instabilities could be generated by these gradients in plasma density if the gradients are strong enough.

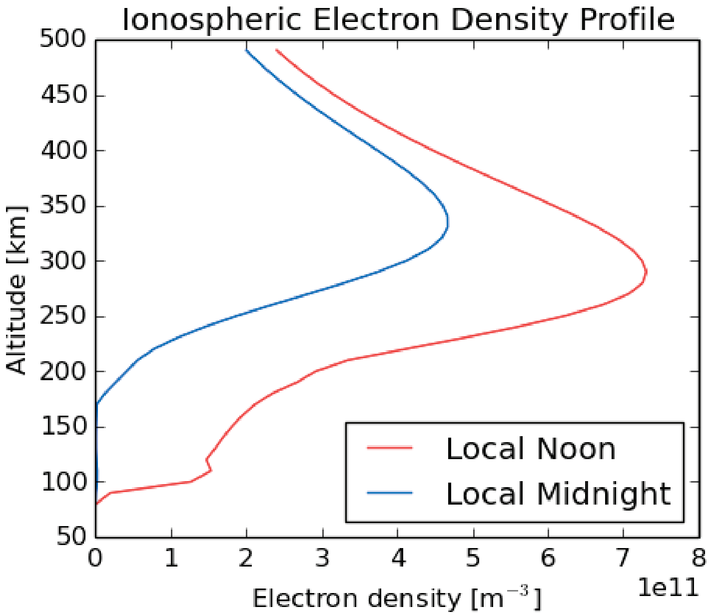

Figure 3. Day vs. Night Electron Density Profiles from the International Reference Ionosphere. During an eclipse, the ionosphere will evolve toward a nighttime density over a much shorter timescale.

Both changes in density and the onset of plasma instabilities associated with eclipses may be detectable by monitoring changes in radio frequency (RF) propagation. The ionospheric refractive index varies with plasma density as well the frequency of the radio wave. Radio waves in the high frequency (HF) band, approximately 3 MHz - 30 MHz, are particularly sensitive to changes in the plasma density of the ionosphere (Seybold 2005). The simplified, general condition for the reflection of radio waves from an ionospheric layer is

$$f_{tx} cos\theta_i = f_{tx} \sin\alpha \leq f_p \approx 9\sqrt{N} \tag{1}$$

where f_{tx} is the frequency of the transmitted RF wave, θ_i is the angle of incidence with respect to the normal to the ionosphere, α is the take-off (elevation) angle of the signal, f_p is the ionospheric plasma frequency in kHz and N is the electron density in cm^{-3} (Hargreaves 1992, Davies 2008). HF signals with frequencies and take-off angles that satisfy equation (1) will be reflected back to Earth, whereas HF signals at a high enough frequency and elevation can penetrate the ionosphere and escape into space. It should be noted that in reality, HF radio signals that return to Earth are often refracted through multiple ionospheric layers before they are re-directed downward, as illustrated in Figure 4.

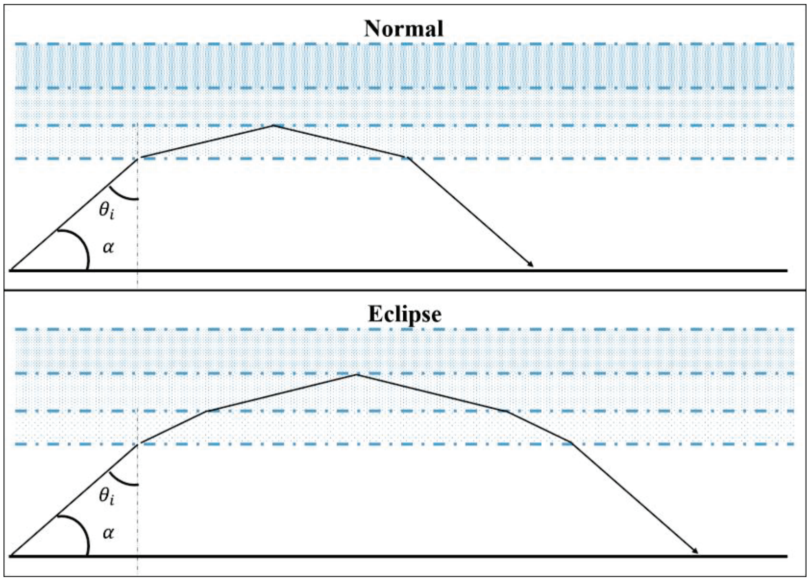

Figure 4. Sketches of radio wave ray paths through normal and eclipsed ionospheres.

As the plasma density decreases over the eclipse, the right side of equation (1) will decrease, lowering the frequency and take-off angle thresholds for radio waves to pass through the ionosphere and escape into space. Additionally, those signals that return to Earth during the eclipse may have to travel further through the ionosphere before they are refracted downwards than under normal conditions as illustrated in Figure 4. Thus, during the eclipse, HF radio waves that do not escape the ionosphere may propagate further than in uneclipsed conditions. Hence, during the eclipse, the maximum usable frequency and the maximum take-off angle for signal return are expected to decrease, while the distance traveled by those returned signals is expected to increase.

The Virginia Tech team designed an observational campaign involving ground-based HF systems to investigate the effects of the eclipse on the plasma density. This included software defined radio systems, coherent scatter radars, and modeling approaches to help understand and assimilate these data into a framework that allows the eclipse effects to be understood in detail.

1.2 Experiment Design

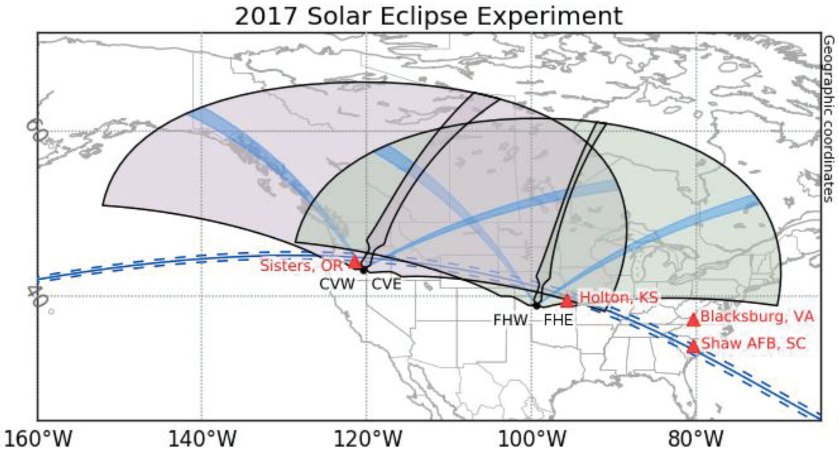

Figure 5. SuperDARN radars' fields of view (magenta and green) and Ionospheric sounders' locations (red triangles) relative to the eclipse's path of totality (blue).

Several ionospheric sounding systems were employed in the 2017 eclipse study. The two systems that were primarily used by the Center for Space Science and Engineering at Virginia Tech (Space@VT) were Super Dual Auroral Radar Network (SuperDARN) radars and temporary ionospheric sounders. The locations of these systems are shown in Figure 5. The SuperDARN radars in Oregon and Kansas provided oblique incidence radar data. The sounders, established at three sites along the path of totality and one in the penumbra, provided vertical incidence radar data.

1.2.1 Temporary Ionospheric Sounders

Figure 6. One of two fan dipole antennas for the ionospheric sounder in Holton, KS

The four temporary, vertical incidence ionospheric sounders were custom designed and built by researchers at Space@VT and the Hume Center. As shown in Figure 5, sounders were deployed at three locations along the eclipse path: Sisters, Oregon; Holton, Kansas; and Shaw Air Force Base (AFB), South Carolina. The fourth sounder used in the eclipse experiment was the prototype sounder, located in Blacksburg, Virginia. Each of these sounders employed an Ettus Software Defined Radio (SDR), amplifiers, filters and two co-located fan dipole antennas. One antenna was used for transmitting and the other for receiving, as shown in Figure 6. Each sounder could only make measurements on one frequency at a time, and they were programmed to step between the operating frequencies of 2.6 MHz, 3.6 MHz, 4.5 MHz and 5.5 MHz.

1.2.2 Super Dual Auroral Radar Network

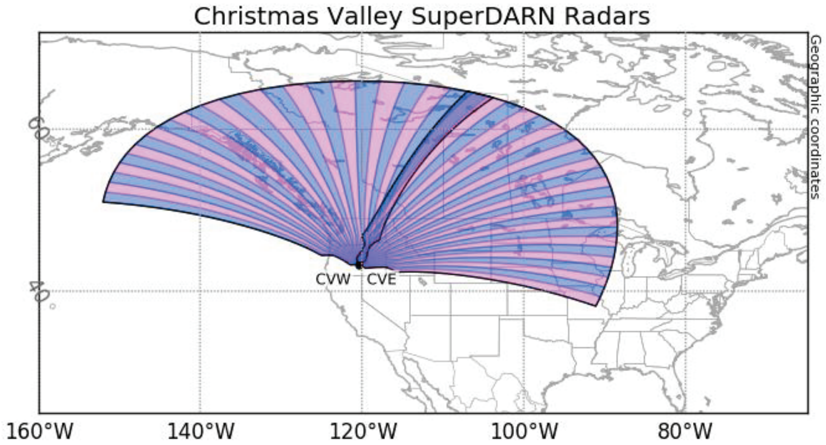

Figure 7. Christmas Valley SuperDARN radars' beams (Blue and Magenta)

SuperDARN is a network of high and mid-latitude coherent HF radars that measure ionospheric irregularities and structures. A dual-radar SuperDARN site has independently operating westward-looking and eastward-looking radars. Each radar employs a phased-array antenna system that is electrically steerable, allowing the radar to form a narrow beam in a given direction. A set of discrete beams forms the fan-shaped field-of-view (FOV) of a SuperDARN site as shown in Figure 7. SuperDARN operates by sending out a pulse on one beam and measuring the returned signal at a later time. From these measurements several quantities can be determined, including the total distance the signal travelled, or slant range. SuperDARN slant range data describe the range (d) in kilometers (km) that the radar signals travel based on the time required for the signal to return to the receiver (Δt), according to the equation:

$$d = \frac{1}{2}\frac{c}{\Delta t} \tag{2}$$

where c is the speed of light in a vacuum. This equation is an approximation, because in reality the propagation speed of the signal varies as it traverses the ionospheric plasma.

All SuperDARN data products are publically available and can be accessed and analyzed using tools in the Data and Visualization Toolkit-Python (DaViTPy) software package. The research presented here is primarily based on the observations of the SuperDARN radars located in Christmas Valley, Oregon and Fort Hays, Kansas, coupled with ray-tracing and geophysical modeling to help understand the physics of the ionosphere during the 2017 eclipse.

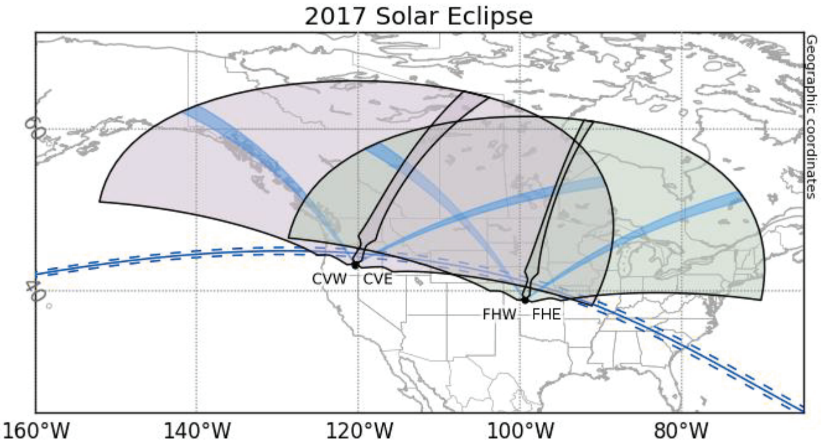

Figure 8. Eclipse path (blue) crossed SuperDARN fields of view (violet and green) and camping beams (indigo).

The SuperDARN radars in Christmas Valley (CV) and Fort Hays (FH) have FOVs that intersect the path of totality of the 2017 eclipse. A SuperDARN radar can only make measurements along a single beam within its FOV at a given time. Hence, when choosing operating modes for the radar there is a trade-off between the temporal resolution along a beam and the spatial resolution across the wide azimuthal FOV. For the eclipse experiment, the Christmas Valley and Fort Hays SuperDARN radars operated on ~10.5 MHz. In order to increase the temporal resolution the systems were run in every-other-beam mode on the eclipse day, completing a full FOV scan through eleven beams every minute. In this mode, the radar made three second measurements on every-other beam, returning to a “camping” beam between successive beams. In each radar scan period there are ten separate three-second measurements along the camping beam. Figure 8 shows the azimuths of the camping beams for the Christmas Valley West (CVW), Christmas Valley East (CVE), Fort Hays West (FHW), and Fort Hays East (FHE) radars. The westward-looking radars made measurements on odd numbered beams and the eastward-looking radars made measurements on even numbered beams. Table 1 shows the azimuths of the beams used by each radar during the eclipse observations. Note that beam azimuth varies by radar sites even for the same beam numbers. (For additional SuperDARN operations summary, see Appendix A.) By skipping every other beam, the temporal resolution of these beams is enhanced without greatly sacrificing the spatial resolution across the FOV.

Beam Number	**Active Beam Azimuths**				**Camping Beam**
	CVW	**CVE**	**FHW**	**FHE**	
0	-	16.74°	-	10.98°	No
1	-	-	-55.78°	-	No
2	-	23.22°	-	17.46°	No
3	-47.54°	-	-49.3°	-	No
4	-	29.7°	-	23.94°	No
5	-41.06°	-	-42.82°	-	No
6	-	36.18°	-	30.42°	No
7	-34.58°	-	-36.34°	-	No

8	-	42.66°	-	36.9°	No
9	-28.1°	-	-29.86°	-	No
10	-	49.14°	-	43.38°	CVE and FHE
11	-21.62°	-	-23.38°	-	CVW and FHW
12	-	55.62°	-	49.86°	No
13	-15.14°	-	-16.9°	-	No
14	-	62.1°	-	56.34°	No
15	-8.66°	-	-10.42°	-	No
16	-	68.58°	-	62.82°	No
17	-2.18°	-	-3.92°	-	No
18	-	75.06°	-	69.3°	No
19	4.3°	-	2.54°	-	No
20	-	81.54°	-	75.78°	No
21	10.78°	-	9.02°	-	No
22	-	-	Not in FOV	Not in FOV	-
23	17.26°	-	Not in FOV	Not in FOV	No

Table 1. Beam azimuths (degrees east of north) of beams with eclipse data for each radar. (Note "-" indicates that the radar has no data from the eclipse period along that beam and "Not in FOV" indicates the beam does not exist at that radar.)

1.3 Modeling

1.3.1 PHaRLAP Ray-trace

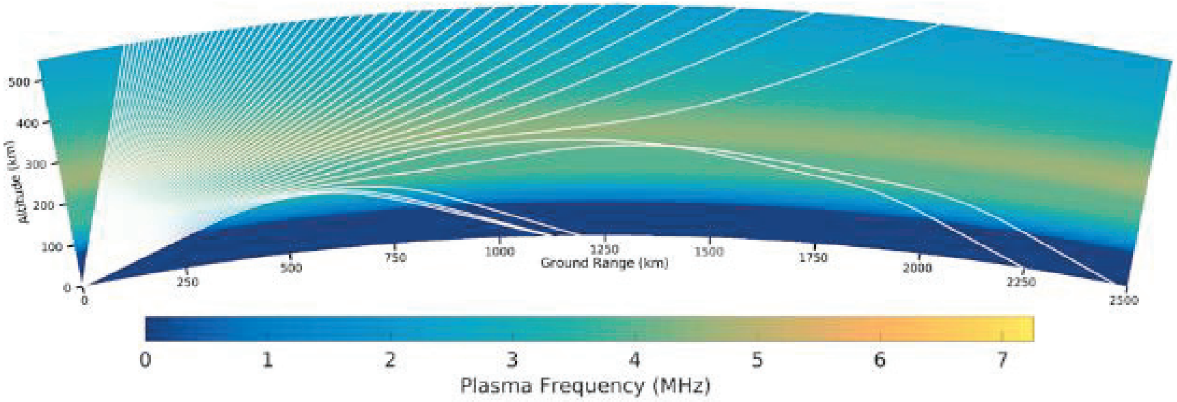

Figure 9. Ray-trace side profile.

Propagation of radio waves can be modeled by ray-tracing, in which the radio wave is treated as a discrete ray propagating through some region of the ionosphere. A ray-trace algorithm calculates the location (*i.e.* range and height) of a ray for each point along its path using the pertinent electromagnetic wave equations. The result is a profile of the radio wave paths at different elevations along a given azimuth, as shown in Figure 9. Ray-tracing can also show refraction in the azimuthal direction, but the vertical refractive effects along a given azimuth are typically larger.

The HF propagation toolbox PHaRLAP (Provision of High-frequency Raytracing Laboratory for Propagation studies) (Cervera and Harris 2011), created by Dr. Manuel Cervera, is a widely used raytracing tool that models propagation through a user-defined model ionosphere. The PHaRLAP ray-tracing codes are compiled Fortran programs that can be called with Matlab wrappers. By specifying initial conditions that correspond to those of a physical radar, PHaRLAP can be employed to generate simulated radar data for comparison with measured data. Later in this thesis we show how this can be used to evaluate the effects of a given eclipse model on HF propagation. We use PHaRLAP to simulate the performance of these SuperDARN radars by employing its two-dimensional ray trace tool and applying it to different model ionospheres.

1.3.2 SAMI

SAMI (Sami is Another Model Ionosphere) is an ionosphere/plasmasphere model developed by the Naval Research Lab. SAMI calculates plasma densities and composition along geomagnetic field lines (*i.e.* along flux tubes) using chemical equations as well as the ion momentum equation, continuity equations, and equations of state for each ion species (Huba, Joyce et al. 2000).

1.3.3 Model Validation

Evaluation of the accuracy of the models was performed by generating simulated SuperDARN data via raytracing through model ionospheres generated by SAMI. The results are then compared to the measured SuperDARN data. An overview of the program that performs this function is shown in the flowchart of Figure 10.

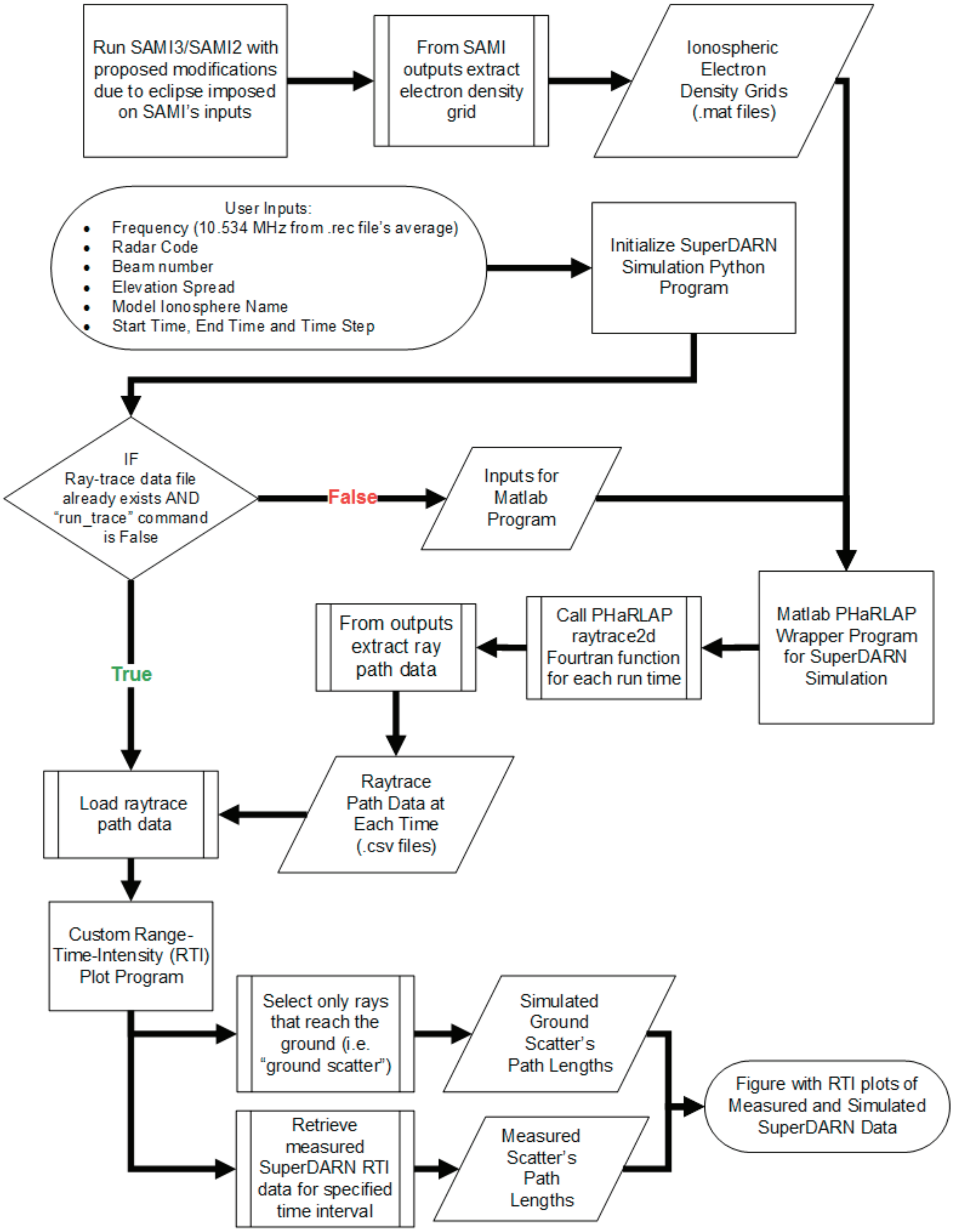

Figure 10. Flowchart of Overall Program Structure of Model

1.4 Structure of the Thesis

The focus of Chapter 1 has been a general overview of the geometry of the 2017 eclipse, a narrow overview of expected eclipse-induced ionospheric changes, and a broad description of our ionospheric eclipse experiment and data analysis techniques. The next chapter details the basic morphology of the mid-latitude ionosphere and the physical effects expected to be important during the eclipse. In the remainder of this thesis after Chapter 2, we will show data taken by SuperDARN coherent scatter radars during the eclipse, and we will interpret the observations in light of the physical effects described in Chapter 2. In order to self-consistently include all of the important physical effects we will use the state-of-the-art computational models described in Chapter 1. The main models to be used are the PHaRLAP ray-tracing algorithm and the SAMI model; the latter was developed by Dr. Joseph Huba at the Naval Research Laboratory. Our focus will be to understand how the ray-paths emanating from the SuperDARN HF radar interact with the eclipsed ionosphere to produce the radar return signatures observed during the 2017 eclipse.

Chapter 2

2.1 Overview of the Ionosphere

2.1.1 The Upper Atmosphere and Ionosphere

The ionosphere is a region of ionized particles that exists in the Earth's upper atmosphere, approximately 60 km-1000 km above ground level. It is important to note that the ionospheric plasma density is several orders of magnitude less than the density of the neutral atmospheric gases over most of this altitude range, as shown in Figure 11. Hence, the neutral particles and winds in this region will influence plasma motion in the ionosphere as detailed in Section 2.2.3. Note that most texts refer to the neutral atmospheric layer at these altitudes as the thermosphere (Rishbeth and Garriott 1969, Banks and Kockarts 1973).

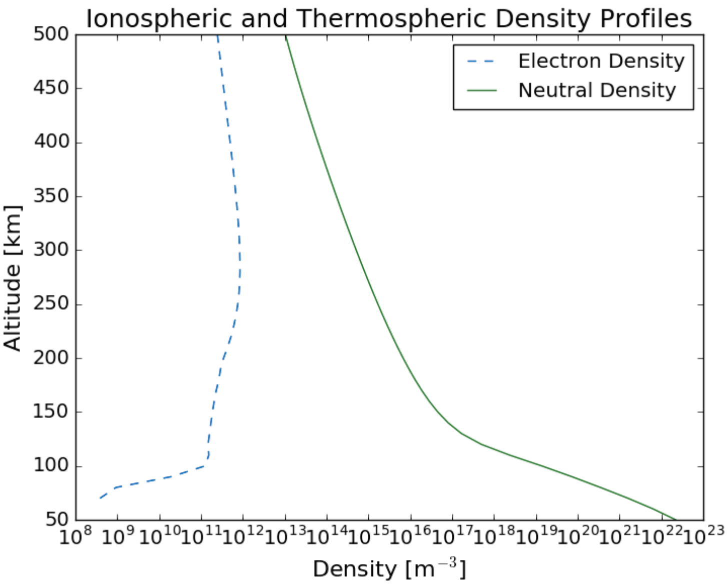

Figure 11. Comparison of Electron Density and Neutral Density in the Upper Atmosphere from the International Reference Ionosphere and the Mass-Spectrometer-Incoherent-Scatter models.

2.1.2 Ionospheric Structure

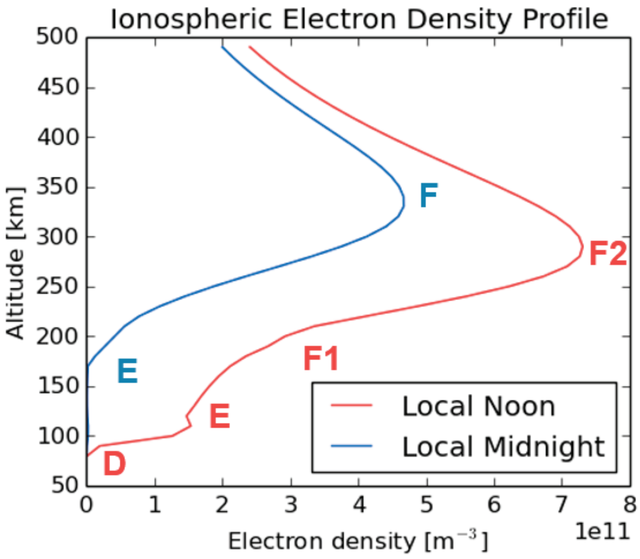

Figure 12. Day vs. Night Electron Density Profiles from the International Reference Ionosphere.

The daytime ionosphere can be divided into four layers, the D layer, E layer, F1 layer and F2 layer as shown by the red curve in Figure 12. The layers are distinguished by their relative plasma densities and their constituents as well as the dominant production and loss processes in each altitude range. The D layer has the smallest plasma density and its plasma is primarily composed of molecular ions. The E layer and F1 layer are composed of a mixture of molecular ions and atomic ions, though the dominant types differ between the two layers. The F2 layer is primarily composed of atomic oxygen ions. Loss processes in the D, E, and F1 layers occur primarily through collisional recombination of ions, and loss in the F2 region is primarily related to diffusion, especially at altitudes above the F2 peak. At night the D layer completely vanishes because the plasma recombines quickly due to high collision rates. The plasma density in the E and F1 layers also decreases rapidly after sunset, leaving a single F layer and weak E layer in the nighttime, as shown by the blue curve in Figure 12. The nighttime persistence of the F layer is due to slow recombination rates, and the transport of plasma from higher altitudes along magnetic field lines into the F layer (Hargreaves 1992).

2.2 Eclipse Physics

In this study, our primary concern is the reaction of the E, F1 and F2 layers during the eclipse, and the effects that changes in the layered plasma structure have on HF propagation. As the main effect of the D layer on RF propagation in the HF frequency range is to attenuate the signal, this omission should not impact our propagation analysis. Hence, we only discuss eclipse physics relating to the E, F1 and F2 layers here.

2.2.1 Overview

The electron density in the ionosphere varies with altitude, season, time of day, latitude, solar activity level, and other factors. The ionospheric density is very dependent on sunlight. Exclusive of plasma dynamics (*i.e.* assuming no plasma motion) and assuming a steady state, the continuity equation for plasma production, q, and loss of plasma is given by the equation:

$$\frac{\partial \mathrm{N}}{\partial \mathrm{t}} = 0 = \mathrm{q} - \mathrm{l}(\mathrm{N}) \tag{3}$$

where l(N) is the plasma loss by recombination as a function of electron density, N, (Rishbeth and Garriott 1969). During an eclipse, q will decrease dramatically as the solar disk is obscured. The imbalance between production and loss should result in a pronounced decrease in electron density during the eclipse, especially at lower altitudes.

However at F region altitudes, the influence of plasma dynamics on the plasma density cannot be ignored. This is especially true at latitudes with a significant magnetic field dip angle, which is defined as the angle between the horizontal plane and the magnetic field vector. The full continuity equation the change in plasma density over time is

$$\frac{\partial \mathrm{N}}{\partial \mathrm{t}} = \mathrm{q} - \mathrm{l}(\mathrm{N}) - \left(\nabla \cdot \mathrm{N}\vec{\mathrm{v}}\right) \tag{4}$$

where $\vec{\mathrm{v}}$ is the net plasma drift velocity (Rishbeth and Garriott 1969). Plasma motion from uneclipsed regions into the eclipsed region along magnetic field lines is likely to be an important mechanism in recovery of the ionospheric plasma density following the eclipse. Plasma dynamics are therefore expected to produce major differences between eclipse-induced ionospheric effects at different magnetic latitudes. In addition to vertical plasma gradients along field lines, there likely will be horizontal plasma density gradients (north-south and/or east-west) due to the non-uniformity of the eclipse obscuration with location and time. If there is a strong horizontal gradient in plasma density or a strong electric field established due to the gradient in charge density, then plasma will diffuse or drift across magnetic field lines. Additionally, the neutral winds in the thermosphere are typically an important driver of plasma motion at mid-latitudes. Hence, the neutral wind-induced plasma motion may be an important mechanism for plasma transport from uneclipsed regions to eclipsed regions. The strength of these differing physical effects will vary with altitude, as well as with the local magnetic field geometry and the solar-zenith angle during the eclipse (see section 2.2.3).

2.2.2 Recombination and Ionization

During eclipse onset, the mechanism with the strongest influence on the ionospheric eclipse response is likely to be recombination of the plasma due to the decrease in sunlight. Recombination rates vary depending on several factors, the most significant of which are composition, species densities and temperature. Since the atmospheric composition, density and temperature vary strongly with altitude, so does the recombination rate. Generally, recombination rates decrease with increasing altitude.

In the E and F1 layers, the production and loss mechanisms are

$$\text{Ionization (I)}: \quad \mathrm{X} + \text{photon} \rightarrow \mathrm{X}^{+} + e^{-}$$

$$\text{Ion} - \text{Neutral interchange } (\gamma): \quad \mathrm{X}^{+} + \mathrm{YZ} \rightarrow \mathrm{XY}^{+} + \mathrm{Z}$$

$$\text{Dissociative recombination } (\alpha): \quad \mathrm{XY}^{+} + \mathrm{e}^{-} \rightarrow \mathrm{X}^{*} + \mathrm{Y}^{*}$$

where X, YZ, Y and Z are elements or molecules, e^- is an electron and the * denotes a neutral particle/molecule in an excited state (Rishbeth and Garriott 1969, Banks and Kockarts 1973). (Note that Y and Z could be two different elements/molecules or the same element.) Disregarding solar zenith angle variations and assuming photoionization of neutral molecules (M) is negligible, the effect of these mechanisms on the electron density (N_e), molecular ion density (N_{M+}) and atomic ion density (N_{A+}) can be represented by

$$\frac{dN_e}{dt} = I[A]n[A] - \alpha N_{M^+} N_e \qquad (5)$$

$$\frac{dN_{A^+}}{dt} = I[A]n[A] - \gamma n[M] N_{A^+} \qquad (6)$$

$$\frac{dN_{M^+}}{dt} = \gamma n[M] N_{A^+} - \alpha N_{M^+} N_e \qquad (7)$$

where α is the dissociative recombination coefficient, γ is the ion-neutral interchange coefficient for the reaction involving the atomic ion A^+ and neutral molecule M, n[M] and n[A] are the neutral densities of M and A, respectively, and I[A] is the photoionization rate coefficient for a given particle (Rishbeth and Garriott 1969). The photoionization rate coefficient for each species is dependent on the ionization cross-section as well as the flux and wavelengths of incoming ionizing radiation.

A simplified initial model of the eclipse effects can be created by assuming a short-lived steady-state condition and assuming charge neutrality to obtain the equation

$$\alpha\beta N^2 - \alpha q N - \beta q = 0 \qquad (8)$$

where N is the electron density, β is

$$\beta = \gamma n[M] \qquad (9)$$

and the production function q is

$$q = I[A]n[A] \qquad (10)$$

(Rishbeth and Garriott 1969). A simple eclipse model of the visible fraction of the solar disk over time (top plot of Figure 13) can be created by calculating the overlap of two identical perfect circles over time assuming one is moving at a constant velocity and the other is stationary. There are several inaccuracies in this simplified model of eclipse obscuration, including but not limited to the absence of the corona, the assumption of a constant velocity for eclipse onset, and the omission of transport terms. However, as Figure 13 shows, there is a significant impact on the ionospheric plasma density due solely to the obscuration of the solar disk.

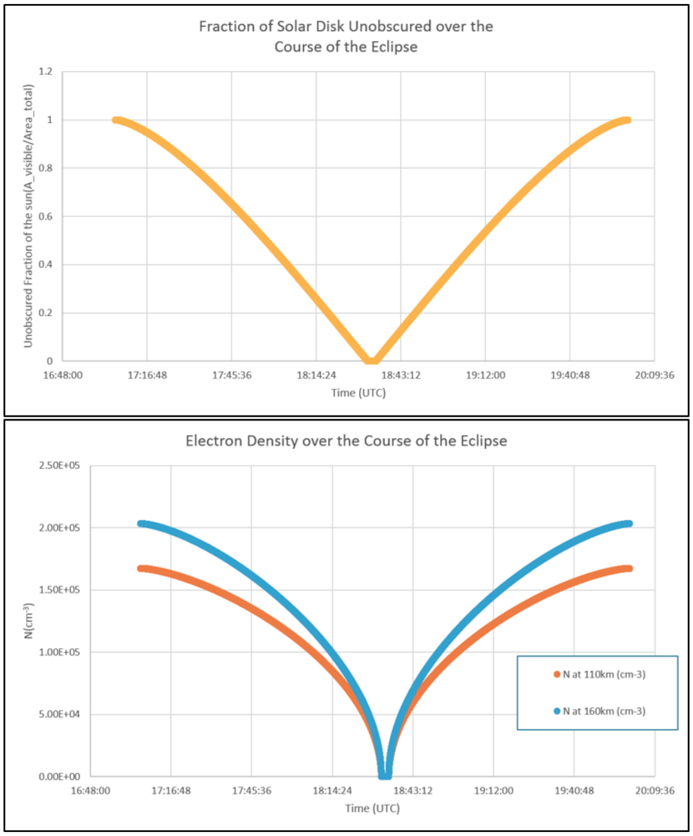

Figure 13. Simple Model of Eclipse Obscuration and the Eclipse Effect on Electron Densities.

Numerical estimates of the recombination timescales for the E and F1 layers are given in Table 2. These timescales indicate the delay of a change in the electron density of an ionospheric layer following a change in q (Rishbeth 1969, Banks and Kockarts 1973). The duration of totality is about one to three minutes depending on location and this is long enough to cause a significant decrease in the E region electron density. Additionally, since the partial eclipse period is about 1.5-3 hours, the recombination timescales are short enough for the eclipse to have a significant impact on the ionospheric E and F1 layer density due solely to the obscuration of the solar disk.

Region	**Time Constant Equation**	**Average Time Constant Calculation**	**Average Time Constant Estimate**
E	$\tau = [2\alpha_D N_e]^{-1}$	$\frac{1}{6}\sum_{z=90km}^{140km}[20^{-7}cm^3s^{-1}\cdot N_e(z)]^{-1}$	~2 minutes
F1	$\tau = [\gamma n[N_2]]^{-1}$	$\frac{1}{6}\sum_{z=150km}^{200km}[6^{-13}cm^3s^{-1}\cdot n[N_2](z)]^{-1}$	~5 minutes

Table 2. Recombination time constants for the E and F layers. (Equations and recombination coefficient values from (Banks and Kockarts 1973). Neutral density values from MSIS and electron density values from IRI.)

2.2.3 Plasma Motion

The net motion of a plasma is actually the sum of all of motions of the individual species of charged particles that comprise it. The motion of each major species as well as its interactions with the other species should be considered. Generally, the motion of an ion in a plasma is due to the Lorentz force, the electric force, collisions with other charged and neutral particles, and gradients in the plasma density and/or the electric and magnetic fields. The steady-state motion of a given species of charged particle, denoted by j, in a plasma can be described by the following equation.

$$0 = \pm q_j n_j \left(\vec{E} + \vec{v_j} \text{ x } \vec{B}\right) - \nabla p_j - m_j n_j \nu_j \vec{v}_j + m_j n_j \nu_j \vec{U} \tag{11}$$

where m_j is the mass of the particle, n_j is the density of the charged particle, q_j is the particle's charge, $\vec{v_j}$ is the velocity of the charged particle, ν_j is the particle's collision frequency, ∇p_j is the pressure gradient, $\vec{U}$ is the neutral wind's velocity, $\vec{E}$ is the electric field and $\vec{B}$ is the magnetic field. For an isothermal plasma with a density gradient (∇n_j), the pressure gradient is

$$\nabla p_j = kT_j \nabla n_j \tag{12}$$

where k is Boltzmann's constant and T_j is the temperature of the species. The velocity of species j is dependent on the pressure due to the gradient in density as well as the forces due to the electric and magnetic fields. Equation (13) shows a steady state equation that relates the velocity of a particle to these disparate forcing terms:

$$\vec{v}_j = \pm \frac{q_j\left(\vec{E} + \vec{v_j} \text{ x } \vec{B}\right)}{m_j \nu_j} - \frac{kT_j \nabla n_j}{m_j n_j \nu_j} + \vec{U} \tag{13}$$

In the eclipse case, the types of motion most likely to be relevant over short timescales are diffusion due to density gradients, ExB drift, and neutral wind forcing.

2.2.3.1 Diffusion

As the eclipse progresses, gradients in the electron and ion densities will lead to motion of plasma into the depleted region from higher density regions. This diffusion process can occur along magnetic field lines (parallel diffusion) or across magnetic field lines (perpendicular diffusion). The velocity of a particle of a species denoted by j due to parallel diffusion is

$$v_{\parallel,j} = -D_{\parallel,j} \frac{\nabla_{\parallel} N_j}{N_j} = -\left(\frac{kT_j}{m_j \nu_j}\right)\left(\frac{\nabla_{\parallel} N_j}{N_j}\right) \tag{14}$$

where $\nabla_{\parallel} N_j$ is the density gradient in the direction parallel to the magnetic field and $D_{\parallel,j}$ is the parallel diffusion coefficient given by

$$D_{\parallel,j} = \left(\frac{kT_j}{m_j \nu_j}\right) \tag{15}$$

(Chen 2016). The velocity of a particle of species j due to perpendicular diffusion is

$$v_{\perp,j} = -D_{\perp,j} \frac{\nabla_{\perp} N_j}{N_j} = -\left(\frac{D_{\parallel,j}}{1 + \omega_{c,j}^2 / \nu_j^2}\right)\frac{\nabla_{\perp} N_j}{N_j} \tag{16}$$

where $\nabla_{\perp} N_j$ is the density gradient in the direction perpendicular to the magnetic field, the gyrofrequency of the particle is

$$\omega_{c,j} = \frac{q_j|\vec{B}|}{m_j} \tag{17}$$

and $D_{\perp,j}$ is the perpendicular diffusion coefficient given by

$$D_{\perp,j} = \frac{D_{\parallel,j}}{1 + \omega_{c,j}^2/\nu_j^2} \tag{18}$$

(Chen 2016). Parallel diffusion is generally more rapid than perpendicular diffusion because it is not affected by cyclotron motion. Hence, we expect parallel diffusion to be the more important of the two in replacing plasma lost via recombination, especially in the umbra region where these losses maximize.

The velocity of plasma particles is determined by the mass and temperature of the species, so the parallel diffusion velocity of electrons in the ionosphere will generally be greater than that of the heavier ions, leading to a local charge imbalance. This imbalance creates an electric field that acts to impede further charge separation via diffusion, but does not stop diffusion. The resulting motion is called ambipolar diffusion, and the diffusion coefficient is

$$D_a = \left(1 + \frac{T_e}{T_i}\right) D_i \tag{19}$$

when $T_e \approx T_i$,

$$D_a \approx 2D_i \tag{20}$$

$$v_{\parallel,j} = -D_{a,j}\frac{\nabla_{\parallel} N_j}{N_j} \approx -2D_{\parallel,i}\frac{\nabla_{\parallel} N_j}{N_j} \tag{21}$$

where the subscript j represents either ions (i) or electrons (e) (Banks and Kockarts 1973, Chen 2016).

In this study we focus on large-scale effects that occur quickly during the eclipse, so we ignore the slower processes in order to study the dominant effects associated with plasma dynamics at F region altitudes.

2.2.3.2 ExB Drift

An electric field causes a charged particle to move along it with the direction it moves depending on the sign of the charge. If a charged particle is in a magnetic field and some component of its velocity is perpendicular to the magnetic field, then the Lorentz force will cause the particle to gyrate clockwise or counterclockwise around the field lines, depending on the sign of the charge, with a radius proportional to the magnitude of the velocity perpendicular to the magnetic field. When an electric field exists with some component perpendicular to an existing magnetic field, then the orbital radius of a charged particle in that region will vary over its orbit as the two fields act on it. Hence the location of the center of the orbit (the guiding center) will move in the direction perpendicular to both the electric and magnetic fields. This motion of the guiding center due to the perpendicular electric and magnetic fields is called ExB drift. The particle's ExB drift velocity is given in the equation bellow (Chen 2016).

$$\vec{v}_{\mathrm{ExB}} = \frac{\vec{E} \times \vec{B}}{B^2} \tag{22}$$

It is important to note that the ExB drift is in the same direction for both positive ions and electrons. Also, since the conductivity parallel to the geomagnetic field at ionospheric altitudes is very large, the parallel E field is effectively zero in the ionosphere.

2.2.3.3 Neutral Winds

Neutral winds also drive charged particle motions in the ionosphere via ion/electron-neutral collisions. As in the case of the electric field, the wind-induced motion of the charged particles will vary with the orientation of the wind vector relative to the magnetic field. The extent of the influence of the magnetic field on wind-induced ion/electron motion will vary with the relative magnitudes of the ion/electron gyrofrequency and the ion/electron-neutral collision frequency. The collision frequencies are a strong function of altitude, so the effects of winds at E region heights can be very different from the effects on motions of particles in the F region.

In regions where the local ion/electron-neutral collision frequency is much greater than the gyrofrequency of a given species, the magnetic field will have negligible influence on the motion of the charged particles compared to the direct influence of the wind through ion/electron-neutral collisions. In contrast, when the local ion/electron-neutral collision frequency is much less than the ion/electron gyrofrequency, then the magnetic field will have a dominant influence on the motion of the wind-driven charged particles. In this case the Lorentz force must be considered. This behavior is summarized by the general equation for the wind-induced drift velocity of a charged species, denoted by j, given below:

$$\vec{v}_{\mathrm{j,w}} = \frac{\nu_{\mathrm{j}}^2}{\omega_{\mathrm{j}}^2 + \nu_{\mathrm{j}}^2}\vec{U} + \frac{\omega_{\mathrm{j}}^2}{\omega_{\mathrm{j}}^2 + \nu_{\mathrm{j}}^2}\frac{(\vec{U} \cdot \vec{B})\vec{B}}{|\vec{B}|^2} + \frac{\nu_{\mathrm{j}}\omega_{\mathrm{j}}}{\omega_{\mathrm{j}}^2 + \nu_{\mathrm{j}}^2}\frac{\vec{U} \times \vec{B}}{|\vec{B}|}. \tag{23}$$

Note that ω_{j} is positive or negative depending on the charge of the species j. There are three components to this motion, one is in the direction of the wind, another is in the direction of the magnetic field, and the third is perpendicular to both the wind and magnetic field vectors.

2.2.3.4 Comparison of Timescales of Plasma Motions

Numerical estimates of the velocities and timescales for the four types of plasma motion discussed in this section are provided in Table 3 for the ions in the F layer. Note that the timescales provided are an estimated of the time it would take a particle to drift 250km[1]. Also, as the parallel and perpendicular diffusion timescales vary with the parallel and perpendicular plasma density gradients, we give approximate diffusion coefficients for each direction from values found in (Rishbeth and Garriott 1969) and then estimate the timescales for each direction assuming $|\nabla_{\parallel}\mathrm{N_j}/\mathrm{N_j}| = |\nabla_{\perp}\mathrm{N_j}/\mathrm{N_j}| = 10^{-3}\mathrm{m}^{-1}$. The estimates

---

[1] The reference distance was arbitrarily set at 250 km as it is wider than the eclipse umbra as well as the E layer and F1 layer.

of the relative timescales for the parallel and perpendicular diffusion coefficients for the same magnitude plasma density gradient show that the parallel diffusion is many orders of magnitude faster than the perpendicular diffusion unless very large density gradient (on the order of at least 10$^{6)}$ is present.

As the partial eclipse period is about 1.5-3 hours, timescales of all of the drift processes given in Table 3, except perpendicular diffusion, indicate that these processes could be play a role in the ionospheric eclipse response. However, the values for the electric field, winds and diffusion might differ from their average values given here during an eclipse. Hence, these estimates only give a rough idea of the types of motion relevant to the ionospheric eclipse response.

Process	**Assumptions**	**Magnitude of Velocity or Diffusion Coefficient**	**Timescale ($\boldsymbol{\Delta t = 250km/\lvert\vec{v}\rvert}$)**
Parallel Diffusion	Diffusion value from (Rishbeth and Garriott 1969).	$D_{\parallel,i} \approx 7x10^6\ m^2/s$ $\lvert\vec{v}_{\parallel,i}\rvert \approx D_{\parallel,i}\left\lvert\frac{\nabla_\parallel N_i}{N_i}\right\rvert$	~(36x10^{-3} sm^{-1})$\lvert N_i/\nabla_\parallel N_i\rvert$ If $\left\lvert\frac{\nabla_\parallel N_i}{N_i}\right\rvert = 10^{-3}\ m^{-1}$ $\Rightarrow \Delta t \approx 36\ s$
Perpendicular Diffusion	$D_{\parallel,i} \approx 7x10^6\ m^2s^{-1}$ $\nu_i/\omega_i \approx 2.7x10^{-3}$ (Values from (Rishbeth and Garriott 1969).)	$D_{\perp,i} \approx 51\ m^2/s$ $\lvert\vec{v}_{\perp,i}\rvert \approx D_{\perp,i}\left\lvert\frac{\nabla_\perp N_i}{N_i}\right\rvert$	~(1.4 hour m^{-1}) $\lvert N_i/\nabla_\perp N_i\rvert$ If $\left\lvert\frac{\nabla_\perp N_i}{N_i}\right\rvert = 10^{-3}\ m^{-1}$ $\Rightarrow \Delta t > 24\ hours$
ExB Drift	$\lvert\vec{E}\rvert \approx 10x10^{-3}\ Vm^{-1}$ $\lvert\vec{B}\rvert \approx 5x10^{-9}\ T$	$\lvert\vec{v}_{ExB}\rvert \approx 200\ m/s$	~21 minutes
Wind-Induced Drift	$\nu_i \ll \omega_i$ $\Rightarrow \vec{v}_w \approx \frac{(\vec{U}\cdot\vec{B})\vec{B}}{\lvert\vec{B}\rvert^2}$ Declination of $\vec{B} \approx 33^o$ $\vec{U} \approx (-\hat{x}55 - \hat{y}38)\ m/s$ (Values from IGRF and HWM models.)	$\lvert\vec{v}_w\rvert \approx 49\ m/s$	~1.5 hours

Table 3. Estimation of velocities and timescales of different ion motions at 300 km.

2.2.4 Solar and Magnetic Geometry

Due to the importance of the local magnetic field orientation to plasma motion, the ionospheric response to an eclipse, especially at F region altitudes, can be expected to vary with magnetic latitude as the magnetic dip angle varies. This has been supported by previous studies such as those discussed in (Bowhill 1969). The 2017 eclipse occurred at mid-latitudes, so downward diffusion of plasma along magnetic field lines into the depleted, eclipsed region of the ionosphere is expected to have a significant impact on the F region plasma density during and after the eclipse. The Millstone Hill radar measured an increase in F region electron density during the July 1963 eclipse relative to that measured on the control day, and hypothesized that it was caused by parallel diffusion of plasma along magnetic field lines into the eclipsed region (Evans 1965).

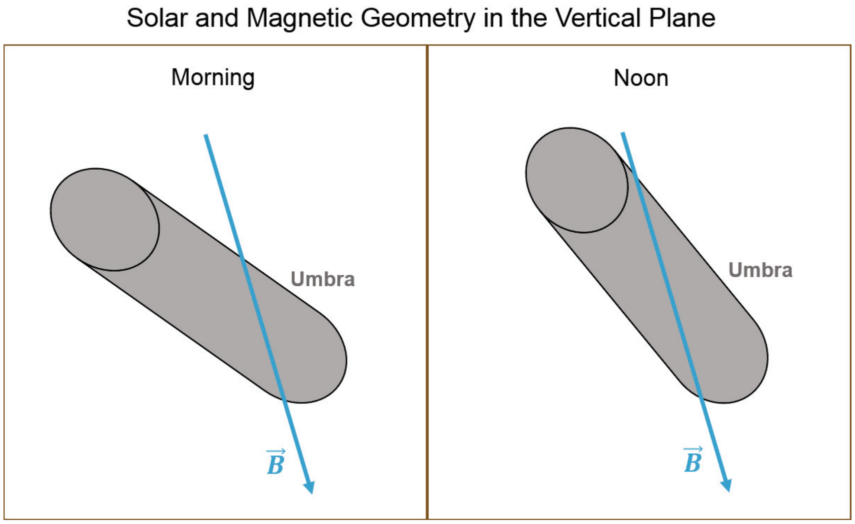

Figure 14. The geometry of the eclipse umbra (gray cylinder) and the mid-latitude magnetic field (blue arrow) in the morning and at noon. The umbra eclipses more area along the magnetic flux tube at noon than it does in the morning.

Additionally, past studies have indicated that ionospheric eclipse responses also vary with the time of day at which an eclipse occurs (Chen, Qi et al. 2013, Chuo 2013, Stankov, Bergeot et al. 2017, Sivakumar 2018). The reason for this is probably two-fold. First, since the structure and density of the ionosphere varies diurnally, the initial state of the ionosphere at the time of eclipse onset depends strongly on the time of day. For example, a noon eclipse would modify an ionosphere near its peak plasma density, whereas an eclipse occurring near sunrise would modify an ionosphere that was initially in a state of low but steadily increasing plasma density. The large differences in the initial states at these different times would be expected to produce significant differences in the ionospheric responses to the eclipse (Chuo 2013).

The second reason for the variation in the ionospheric eclipse response variation with local time is the effect of the orientation of the sun relative to the magnetic field. The plasma content on a particular flux tube that passes through the eclipsed region will depend on the angle of the sun-Earth line relative to the flux tube. If the line between the Earth and the sun is nearly aligned with the geomagnetic field, as illustrated in the right panel of Figure 14, then the eclipse would deplete most of the plasma in the flux tube (along the field line). In contrast, if the sun is not well aligned with the local magnetic field, as shown in the left panel of Figure 14, then the eclipse would not deplete as much of the plasma in the magnetic flux tube, so diffusive refilling of the eclipsed ionospheric region could occur more rapidly. Therefore, the effect of the eclipse is expected to vary with size of the solar zenith angle (the angle of the sun relative to directly overhead), as well as the magnetic field angle (Stankov, Bergeot et al. 2017). Hence, both the time of year and the time of day are likely to impact the eclipse responses at mid and high latitudes, where the magnetic field has a significant dip angle.

Chapter 3

3.1 SuperDARN Operation and Data Visualization

3.1.1 Overview

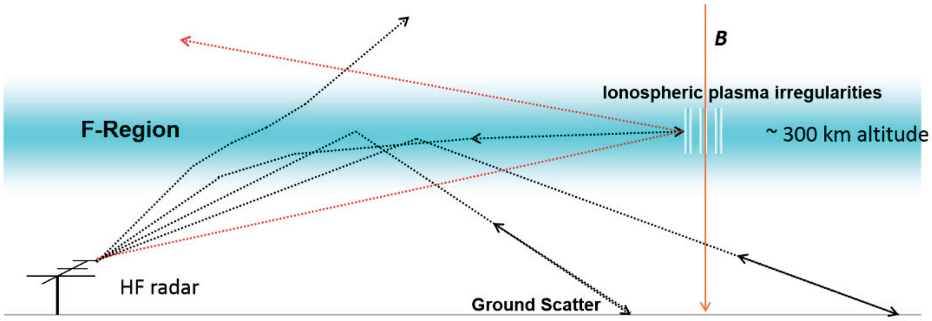

Figure 15. Diagram of the two primary types of scatter modes observed by SuperDARN radars. (Figure from (Ruohoniemi 2012). Used with permission of author.)

As discussed in section 1.2.2, a SuperDARN radar sends out a pulse and measures the scattered signal that returns to the radar from various ranges. SuperDARN primarily measures two types of scatter, ground scatter and ionospheric scatter, illustrated in Figure 15. Ionospheric scatter occurs when the outgoing ray is reflected back to the radar from a plasma structure in the ionosphere. In contrast, ground scatter signals are refracted through and/or reflected from the ionosphere down to the ground, where it is they are reflected back towards the radar. Signals with low Doppler velocities and small spectral widths are typically flagged as ground scatter (Nishitani, Ruohoniemi et al. 2019).

SuperDARN radars bin the measured scatter by time of arrival, corresponding to bins of ranges from the radar called “range gates”. The size of these range bins (ΔR) is typically about 45km, with the first range gate located about 180km from the radar (Nishitani, Ruohoniemi et al. 2019). Hence, slant range is related to range gate number by

$$R_{slant} = R_0 + \left(n_{gate}\right)(\Delta R) \Leftrightarrow n_{gate} = \frac{R_{slant} - R_0}{\Delta R} \tag{24}$$

where R_0 is the range of the first range gate. Several quantities can be detemined from the radar’s measurments including signal-to-noise ratio (SNR), Doppler line-of-sight velocity, spectral width of the signal and elevation (not availible from Fort Hays radars) (Nishitani, Ruohoniemi et al. 2019). These data are typically downloaded and plotted using the DavitPy software toolkit.

3.1.2 Eclipse Data Visualization Methods

One of the most common methods of presenting SuperDARN data is a Range-Time-Intensity (RTI) plot, shown in Figure 16. In a RTI plot, the range of each datum from the radar (in range gates or slant range) is plotted over time with the color of each datum indicating the observed value (*i.e.* SNR, velocity, *etc.*). RTI plots generated with DavitPy functions also include top panels with plots of additional data on the radar’s operation and local conditions such as sky noise. For the eclipse study, we added an additional panel to these top panels to plot two eclipse parameters over time. In this work, these parameters are the distance of the eclipse center on the ground from the radar and the azimuth of the line on the ground connecting the eclipse center and the radar. It is important to note that these eclipse parameter plots only give a general representation of the times of the eclipse onset, maximum and end for comparison to measured data. A representation of how the eclipse magnitude varies over the entire beam would be very difficult to display alongside these data, although it might yield greater insight into the difference in eclipse conditions at different beam azimuths and radar sites (see section 3.3.2).

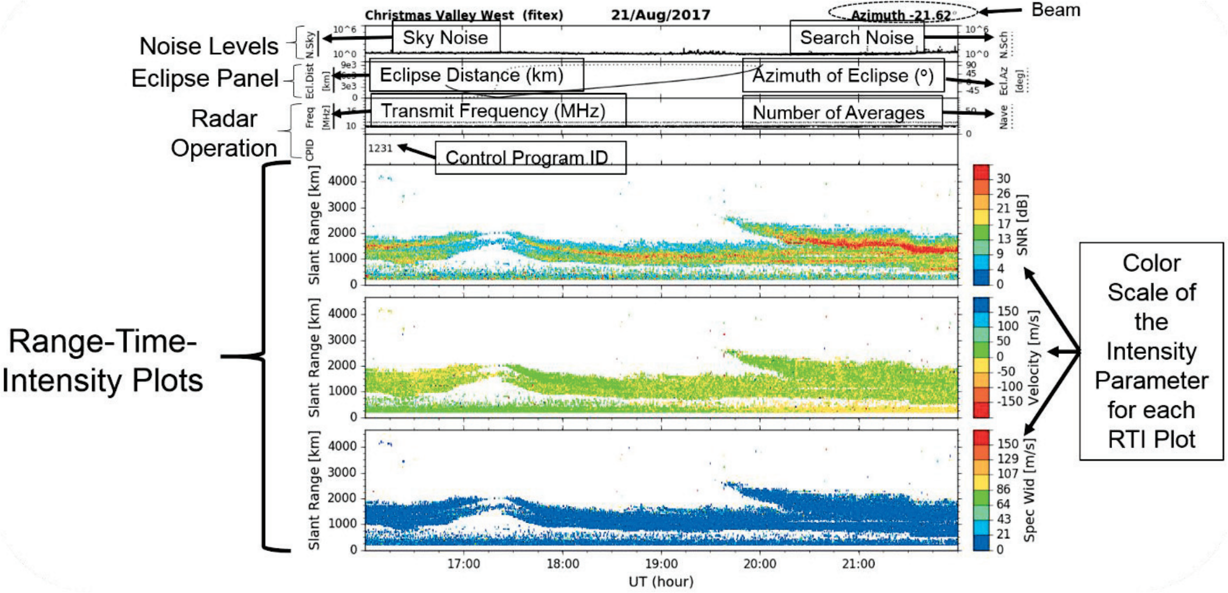

Figure 16. Example Range-Time-Intensity (RTI) plot from DavitPy for the Christmas Valley West eclipse day camping beam. The parameter plotted on the y-axis of each of the top plots is indicated by the text box and arrow.

RTI plots are an excellent data presentation method for a single beam. DavitPy offers a fan plotting tool for visualizing data across the FOV; however, a fan plot can only show data from a single time. In order to qualitatively show the magnitude and timescales of the measured eclipse responses across the FOV of the radar, we created a custom visualization, reffered to here as a Scatter-Time-Azimuth (STA) plot. As shown in Figure 17, a STA plot consists of overlayed lineplots, where each line shows the average/statistical value of a beam's observed data over time, for all beams in the FOV with data.

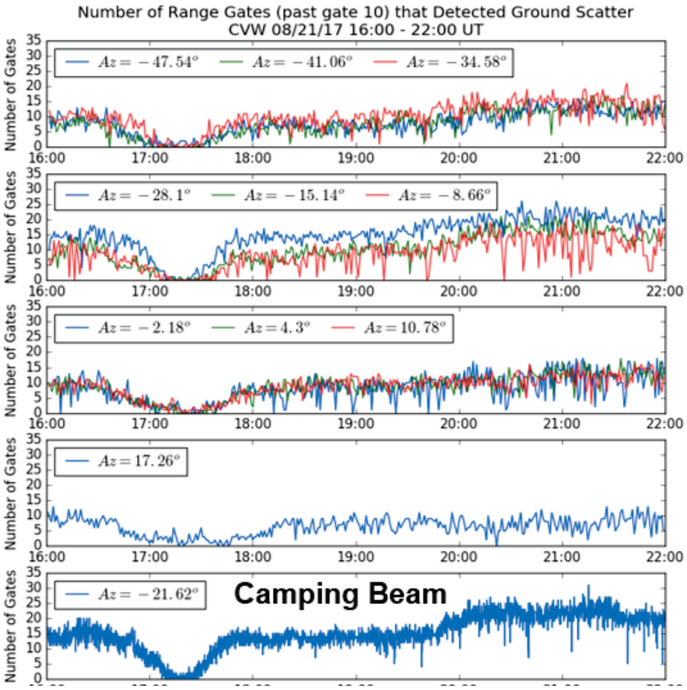

Figure 17. Example Scatter-Time-Azimuth plot for the Christmas Valley West radar on eclipse day.

3.2 SuperDARN Eclipse Data

3.2.1 SuperDARN Eclipse Operation

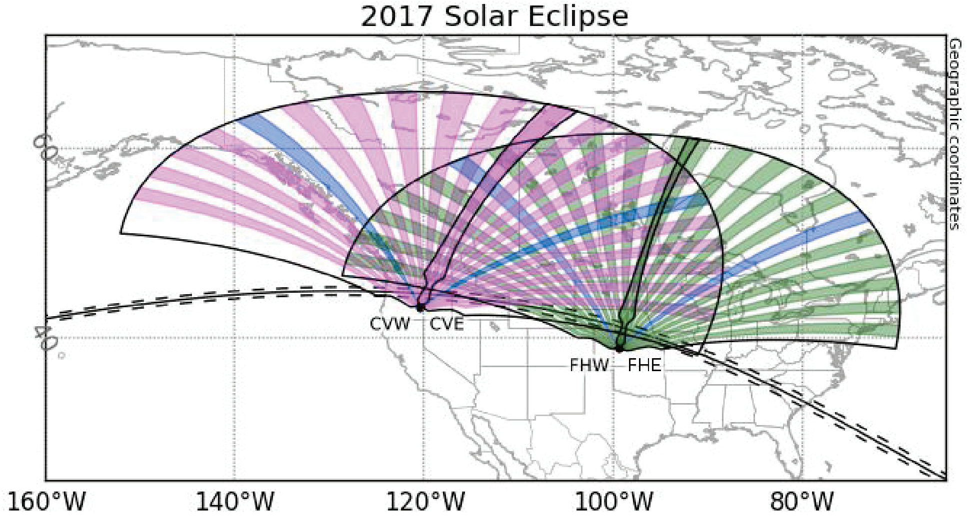

Figure 18. Beams intersecting the eclipse path (black) that made measurements during the eclipse at the Christmas Valley (magenta and blue) and Fort Hays (green and blue) SuperDARN radar sites. Camping beams are highlighted in blue.

As described in section 1.2.2, on eclipse day the SuperDARN radars in CV and FH operated in every-other beam mode at about 10.5 MHz. In this mode, a radar makes measurements on every-other beam (highlighted magenta and green in Figure 18), returning to the “camping” beam (highlighted blue in Figure 18) between successive beams. Hence, this operating mode maximizes the temporal resolution of these data for each camping beam with only a small sacrifice in spatial resolution across the FOV. Figure 18 illustrates the spatial coverage of each beam with eclipse data. The radars started operating in this mode around 12:00 UT on August 21 and continued operating in this mode until around 0:00 UT on August 22.

It is worth noting in Figure 18 that the path of the eclipsed umbra region passed very close to the radar sites at both FH and CV. The portion of the ionosphere observed by the radars was therefore mainly on the penumbra of the eclipse. Based on Figure 18 the only exceptions to this were the most eastward-directed beams at CV and the westward beams at FH.

3.2.2 Camping Beams' Data

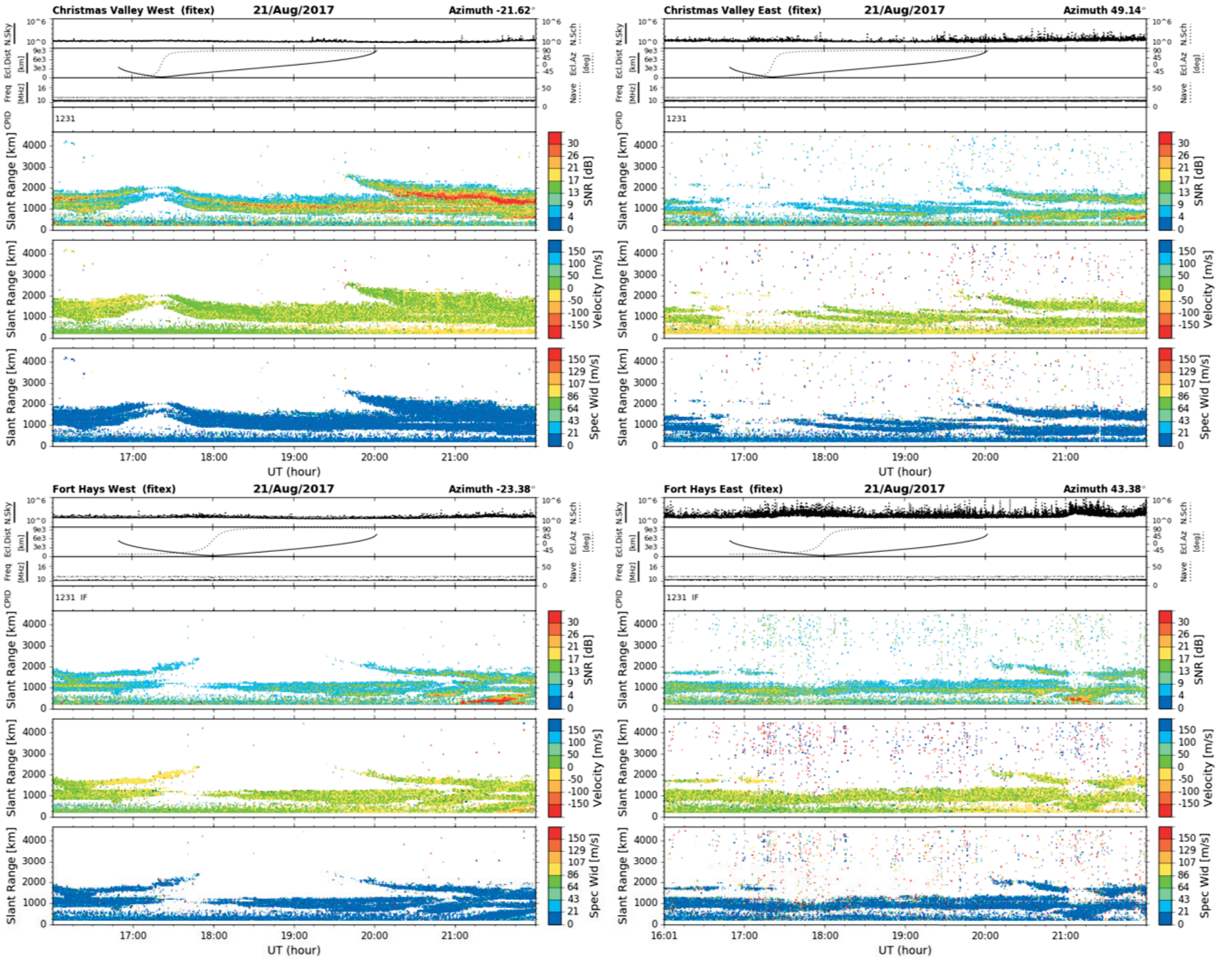

Figure 19. RTI plots of data from camping beams of SuperDARN CVW, CVE, FHW and FHE radars. The eclipse occurs between about 17UT to about 20UT with the eclipse center passing closest to CVE/CVW at about 17:30 UT and closest to FHE/FHW at about 18 UT.

The RTI plots in Figure 19 show data from the camping beams during the eclipse experiment. In all cases the observed scatter from ranges less than ~630 km[2] (*i.e.* before range gate 10) is fairly constant during the eclipse. Here we use the word "scatter" to refer to signals observed at ranges beyond the 630 km range gate. The low spectral widths and velocities shown in Figure 19 indicate that the majority of scatter measured on the eclipse day is E region and/or F region ground scatter, not ionospheric

---

[2] Scatter from slant ranges less than 630 km, commonly seen in SuperDARN data, are typically classified as meteor scatter (*i.e.* scatter from ionization created by meteors) and/or sporadic-E scatter (linked to neutral turbulence in the lower E region) (Nishitani, N., J. M. Ruohoniemi, M. Lester, J. B. H. Baker, A. V. Koustov, S. G. Shepherd, G. Chisham, T. Hori, E. G. Thomas, R. A. Makarevich, A. Marchaudon, P. Ponomarenko, J. A. Wild, S. E. Milan, W. A. Bristow, J. Devlin, E. Miller, R. A. Greenwald, T. Ogawa and T. Kikuchi (2019). "Review of the accomplishments of mid-latitude Super Dual Auroral Radar Network (SuperDARN) HF radars." Progress in Earth and Planetary Science **6**(1): 27.).

scatter. Thus, the observed changes in range are likely changes in the signal path length through the ionosphere rather than the appearance or disappearance of an ionospheric irregularity. It is noteworthy that the observed scatter ranges are “clustered” into two groups or “scatter bands”. These likely represent refraction of the signals through two different trajectories through the ionosphere, which coincide with different beam elevations, and therefore different angles of incidence on the bottomside ionosphere. These relationships between the range gates and the incidence angle will be made clear in the next chapter, where ray-tracing results are shown. The two scatter bands might represent E region scatter vs. F region scatter (*i.e.* reflection from different altitudes) and/or single-hop propagation vs. multi-hop propagation (*i.e.* how many times does the ray pass through the ionosphere and down to ground before it is reflected back to the radar).

The observed eclipse response varies with radar site, time and and look direction. The variation of observations with look direction will be more closely examinined in the following section. In all cases, less scatter is observed during the eclipse period, indicating that much of the transmitted energy that would normally reflect back to the receivers is lost during the eclipse. However, the data from eastward-looking camping beams show a weaker eclipse signature than data from westward-looking camping beams, whose eclipse signature includes a change in slant range. However, these plots show a much stronger eclipse signature in data from westward-looking camping beams than data from eastward-looking camping beams. Both the CVW and FHW camping beams observed an increase in the path length of scattered signals during eclipse onset, although the timescales differ slightly between the two sites. Post-totality, the CVW camping beam observed a steady recovery to pre-eclipse conditions that was symmetric with the eclipse onset about the time of eclipse maximum. However, the FHW camping beam did not observe a symmetric recovery to pre-eclipse conditions after totality relative to the eclipse maximum. The possible reasons for this will be discussed in section 3.3.3 and in following chapters.

3.2.3 Summary of Data Across the Field-of-View

As the plots of Figure 19 show, the radar signatures varried with location as well as look direction. In order to further examine the magnitude and timescales of the measured responses of the various beams and radars, the number of range gates with measured ground scatter were plotted over time for each beam with data in a multi-pannel STA plot. In order to focus on the eclipse effect, only ranges beyond ~630 km are plotted as scatter in Figure 20. This is resonable because data from shorter ranges are nearly constant during the eclipse[3]. Finally, data from the camping beam of each radar is plotted in a separate subplot at the bottom of the STA plot for the radar.

---

[3] As sporadic-E and meteor scatter are characterized by the conditions in the mesosphere (*i.e.* the neutral atmosphere from ~30km to ~100km), data from these scatter modes does not provide insight into eclipse-induced changes in the upper E region (above ~120km) and in the F region.

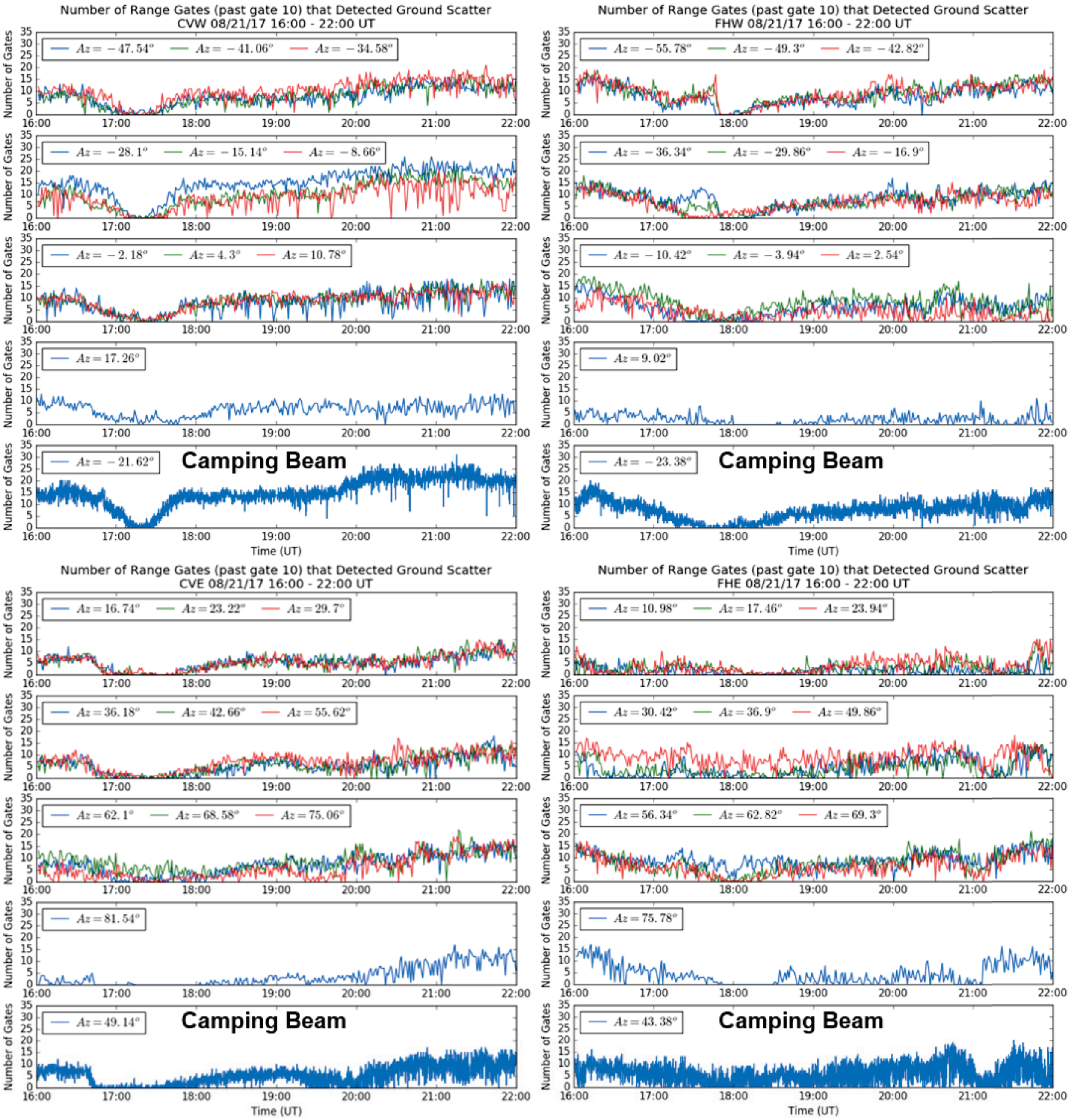

Figure 20. Summary of ground scatter behavior across beams (labeled by azimuth) of all radars.

Figure 20 confirms that the eclipse response, indicated by decreases in the amount of ground scatter received, varies with radar look angle as well as with location and time. Generally, the eclipse response measured by the radar can be seen to decrease as the radar looks away from the west and towards the east. Additionally, for those radars that observed an eclipse response, the data from the pre-totality and post-totality periods are only symmetric in the CVW data, except for azimuth 17.26^o. In all other cases, these data from the pre and post-totality periods are asymmetric in time.

3.2.4 Beams Aligned with the Magnetic Field

The magnetic field orientation is an important factor in the eclipse response, so data from azimuths that are most nearly aligned with the declination of the local magnetic field should be examined closely. At CV the magnetic declination is about 14.31° and at FH the magnetic declination is about 4.79°. The active SuperDARN radar beams that are most closely aligned with geomagnetic flux tubes are those at 16.74° at CV (CVE beam 0) and 2.54° at FH (FHW beam 19). These beam data are shown in the RTI plots of Figure 21. There is a slight path lengthening observed in the CVE beam data, though during the maximum eclipse most of this scatter disappears. FHW data show even less of an effect, with only some diminished scatter during the eclipse. However, these data will be important in subsequent analysis and so are included here.

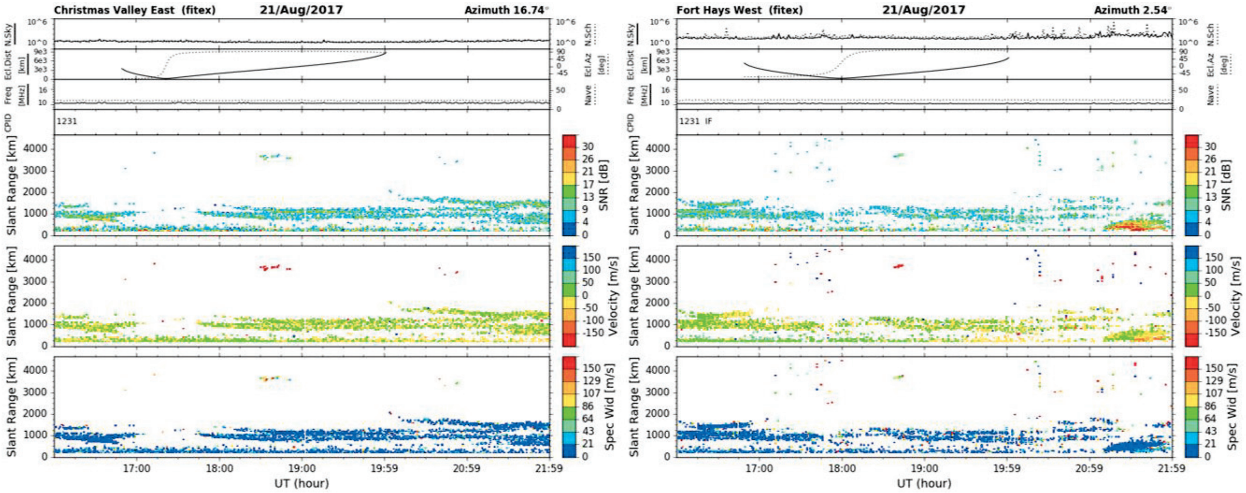

Figure 21. RTI plots of data from the SuperDARN beams best aligned with the declination of the local magnetic field at each radar.

3.2.5 Christmas Valley Radars' Angle of Arrival Data

As mentioned in section 3.1.1, the Christmas Valley SuperDARN radars also measured the elevation angle of returned scatter. These data are plotted in Figure 22 for the CVW and CVE camping beams, CVE 16.74° (closest to magnetic alignment) and CVW 17.26° (the closest CVW beam to CVE 16.74°). The color scales indicate the elevation angles, so these data show that the elevation angles of returned scatter are mostly low, especially for CVW -21.62°. Additionally, the range of scatter from higher elevations appears to increase and mostly disappear around maximum eclipse, leaving only scatter from lower elevations. This suggests that the signals at higher elevations may escape the ionosphere or travel further than the maximum range SuperDARN can measure. At the same time, the slant range of scatter from these lower elevations increases. This could be due to a change in the reflection height of these signals from the E layer to the F layer.

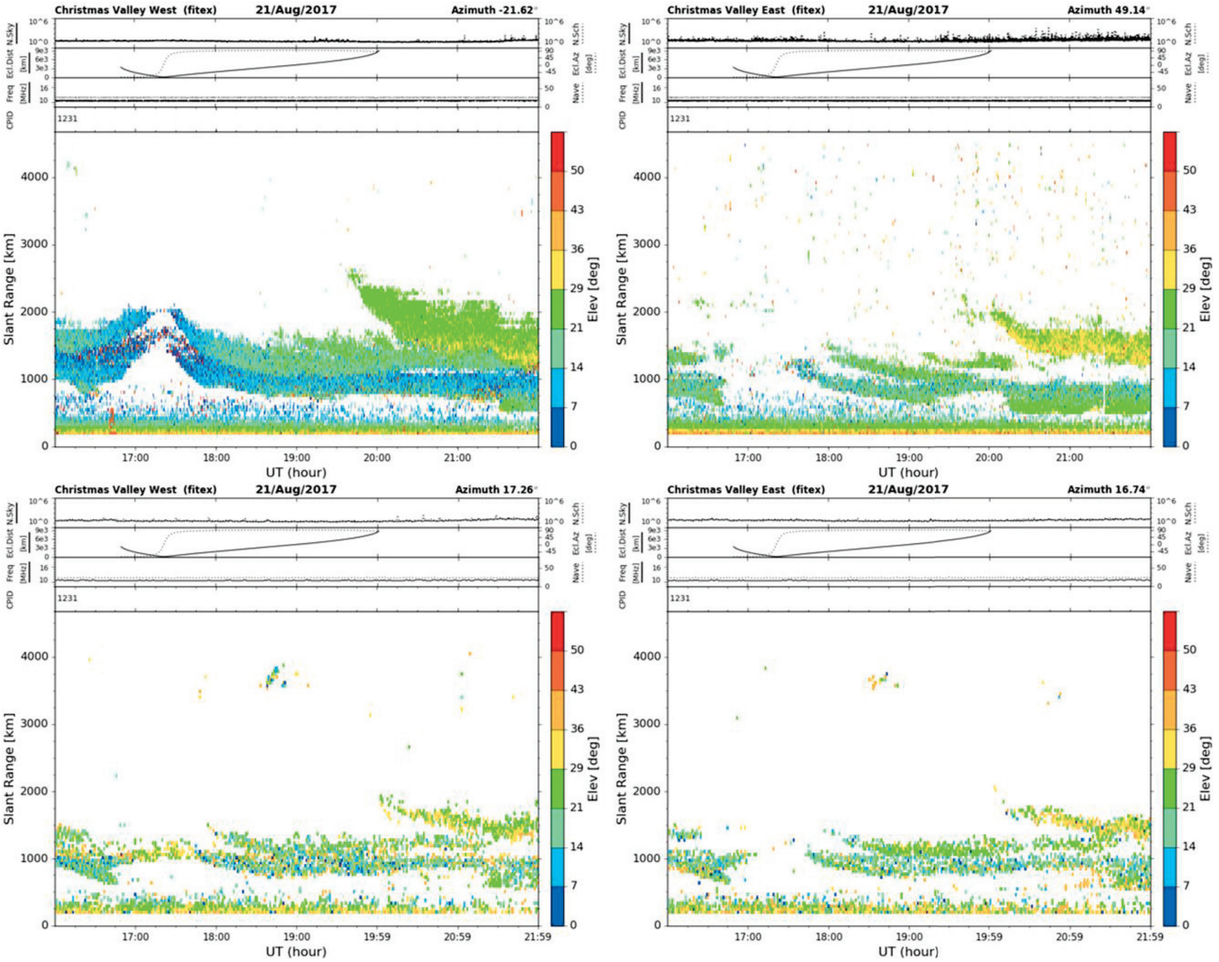

Figure 22. Elevation RTI plots Christmas Valley for camping beams and azimuths closest to the magnetic declination.

3.3 Preliminary Analysis and Research Questions

3.3.1 Key Observations and Questions

Key features of these data presented in Section 3.2 are summarized in Table 4 below.

Data	Features	Figures
Camping Beam Data	• Most scatter measured has low velocity and low spectral width, indicating that ground scatter constitutes the majority of the measured scatter. • Decrease in the amount of observed scatter around time radar closest to the eclipse center.	• Figure 19 • Figure 19
CVW Camping Beam	• Path lengthening during eclipse onset • Fairly symmetric return to pre-eclipse path lengths after totality. • Low elevation angles at greater range gates measured on returned scatter during the eclipse.	• Figure 19 • Figure 19 • Figure 22

FHW Camping Beam	• Path lengthening during eclipse onset. • Recovery appears to take longer than at CVW and is not symmetric with the onset phase with respect to time of eclipse maximum.	• Figure 19 • Figure 19
CVE Camping Beam	• Loss of scatter return during onset of eclipse. • Scatter "bands" return after eclipse center has come closest to the radar. These path lengths then decrease as eclipse recedes. • Low elevation angles measured on returned scatter during the eclipse.	• Figure 19 • Figure 19 • Figure 22
FHE Camping Beam	• Slight decrease in returned scatter as eclipse center nears the radar. However, eclipse effects are not pronounced.	• Figure 19
STA plots of the number of ground scatter points each radar observed (past the 630km range gate)	• The decrease in the number of scatter returns measured by the radar associated with the eclipse can be seen to decrease as the radar looks away from the west and towards the east. • Data from many beams have a recovery that is asymmetric in time with the observed eclipse onset response. The exception is CVW azimuths -47.54 to 10.78°.	• Figure 20 • Figure 20
CVE 16.74°	• Slight lengthening of returned path lengths during onset with a loss in signal around closest eclipse point. Fairly symmetric return to pre-eclipse conditions post-totality. • Low elevation angles measured on returned scatter during the eclipse.	• Figure 21 • Figure 22
FHW 2.54°	• Slight loss of scatter as eclipse center nears the radar, especially at longer ranges.	• Figure 21

Table 4. Summary of key features observed by SuperDARN radars during the eclipse.

There are many questions raised by these data that invite further analysis. In this thesis we focus on four:

1. Are the increases in path lengths observed during the eclipse due to changes in the altitude of peak plasma density, or due to ducting of the signals through the region where plasma is depleted?
2. Why do data from different sites appear to be so different?
3. How can numerical models and ray-tracing algorithms be used to help understand the observed SuperDARN radar data measured during the eclipse?
4. How might the direction and magnitude of thermospheric winds affect the signals observed by the radars?

3.3.2 Analysis Considerations and Challenges

Any analysis of ionospheric data obtained during an eclipse must take into account the variation in solar occultation with altitude and time. When looking at the SuperDARN data, the analysis is further complicated by the fact that the system is an oblique sounder, meaning that we must take into account how the eclipse conditions vary with range from the radar as well as with altitude and time. Additionally, the eclipse geometry relative to the various radar beams differs by site, as illustrated in Figure 18. This will make comparison between the two sites more complex.

This difference in the eclipse geometry might account for some of the differences observed in these data. However, there are additional differences between the two sites that may be significant. For example, the eclipse occurred in the morning at Christmas Valley, whereas it occurred around midday at Fort Hays. As discussed in section 2.2.4, the time of day at which an eclipse occurs is expected to have a significant effect on the ionospheric response to the eclipse. In this case, the ionosphere at Christmas Valley was likely still in a state of growth when the eclipse began, but the ionosphere at Fort Hays was likely near its peak density. The magnetic field geometry with respect to the solar zenith angle is also somewhat different at each site. As discussed in section 2.2.4, such a difference could affect the time scales over which the ionosphere recovers from the eclipse.

In order to answer the questions posed here, a more rigorous analysis is needed. Comparison between ionospheric model outputs and these observed data is essential for this analysis. Our analysis method and results are discussed in the following chapters.

Chapter 4

4.1 Method for Evaluating Ionospheric Models

4.1.1 Overview

An ionospheric model is validated by comparison to measured data. In this study, the models of the eclipsed ionosphere were generated by imposing conditions on the SAMI model ionosphere (Huba, Joyce et al. 2000, Huba, Joyce et al. 2008). SAMI's outputs include the electron density at various latitudes, longitudes, times and altitudes. Simulated SuperDARN data were then obtained by raytracing through these electron density profiles. The focus of this chapter is to present methods of comparing model data to measured SuperDARN data and to employ these methods to evaluate the output variations under different model conditions. Through this process we will identify the conditions that produce the best agreement with measured SuperDARN data.

4.1.2 SAMI Data

As discussed in section 1.3.2, SAMI is a model ionosphere that calculates plasma densities and composition along magnetic flux tubes (Huba, Joyce et al. 2000). There are two different SAMI models, SAMI2 and SAMI3, both of which were employed in this study. SAMI2 is a two-dimensional version of SAMI that calculates plasma and neutral parameters along a single flux tube. SAMI3 is a three-dimensional version of SAMI, initialized using the output of SAMI2, that calculates these parameters along multiple flux tubes (Huba, Joyce et al. 2008). The output parameters are intrinsically given in magnetic coordinates, not geographic coordinates (Huba, Joyce et al. 2000, Huba, Joyce et al. 2008). Hence, the electron density grids of SAMI2 and/or SAMI3 must be interpolated to produce grids in geographic coordinates for raytracing. These interpolated electron density grids are the input model ionospheres that are used for ray-tracing. As discussed in section 1.3.2, SAMI models of the eclipsed ionosphere were generated by imposing various masks on the input EUV flux, as well as modifying other input parameters (Huba and Drob 2017). These modifications will be discussed in more detail in the following sections and chapters, but the general process is outlined in Figure 23.

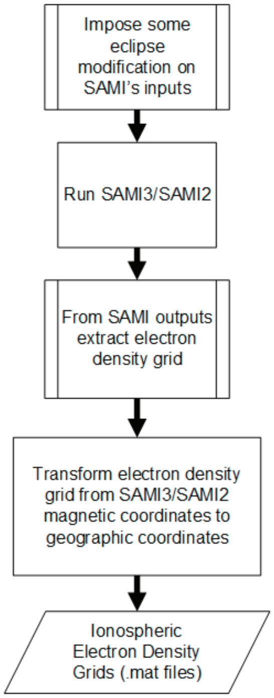

Figure 23. Flowchart of process to generate an input ionospheric model for ray-tracing.

4.1.3 SuperDARN Ray-trace Simulation

In section 1.3.1, the use of the PHaRLAP ray-trace toolbox to model the propagation of a radio signal through a model ionosphere is described. Simulated SuperDARN data can be extracted from the output of a ray-trace that is initialized with the radar operating parameters (*i.e.* operating frequency, elevation spread, beam azimuth, latitude, longitude, *etc.*). In practice, the operating parameters for the SuperDARN radars and beams are found using DavitPy functions, then these conditions are imposed on a customized PHaRLAP MATLAB wrapper function that runs the ray-trace algorithm. A full version of the code is too large to show in a single flowchart, so two flow charts will be used in the following paragraphs to illustrate the algorithms.

As shown in Figure 24, the ray-trace algorithm takes inputs from the Python program and traces the propagation of all rays in the list of elevations for each time, radar and beam input. For each time, the files containing the corresponding output SAMI data are loaded into the program. For each beam of each radar, the program uses a gridded interpolation to make a “slice” of the ionosphere along the azimuth corresponding to the beam for all specified ranges and altitudes. Then the raytrace2d Fortran function is called with the electron density grid, initial conditions and distinct ray elevations as inputs. Each elevation angle corresponds to a different ray that the function traces until any of the following occur: the ray exits the ionospheric grid; the ray hits an irregularity; or the ray reaches the ground after the specified number of hops. In the SuperDARN simulation the hop limit is set to one and multi-hops are assumed to be negligible; it will be shown a-posteriori that this is a reasonable assumption.

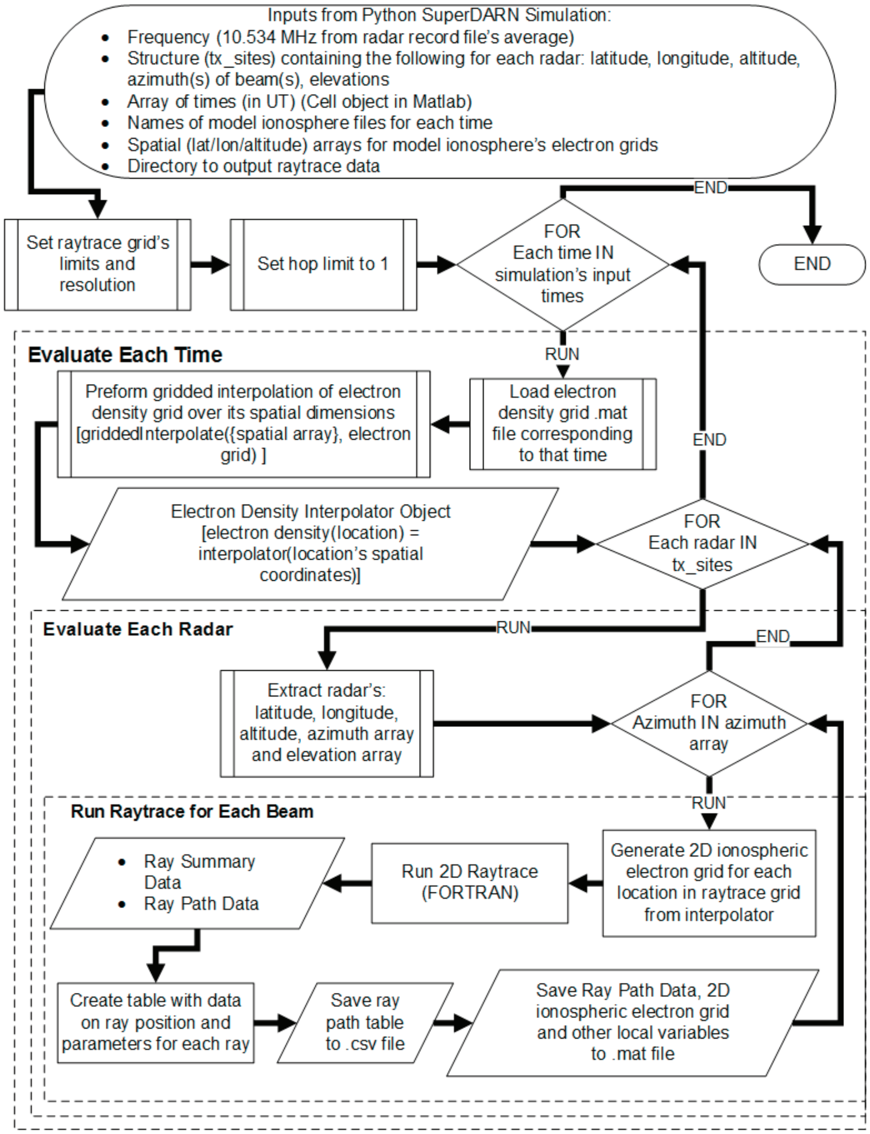

Figure 24. Flowchart of SuperDARN PHaRLAP-based ray-trace algorithm.

The algorithm shown in Figure 25 demonstrates how the ray-tracing code is used to model the SuperDARN radar. Additional details are given in Appendix B. As illustrated, the program finds the operating parameters of the input SuperDARN radar(s) and beam(s) and checks if a ray-trace has already been run. If not, the code calls the PHaRLAP wrapper with the appropriate inputs before proceeding. The ray-trace path data are loaded from the files into a data frame, filtering out any ray path data from rays that do not return to the ground. Finally, the path length is extracted for each of the paths for each time, along with other parameters that are analogous to measurements by the SuperDARN radars (*i.e.* elevation angle, *etc.*). These data are binned into range gates. Values in the same range gate are averaged or counted (depending on the parameter). Finally, these data are stored for future use.

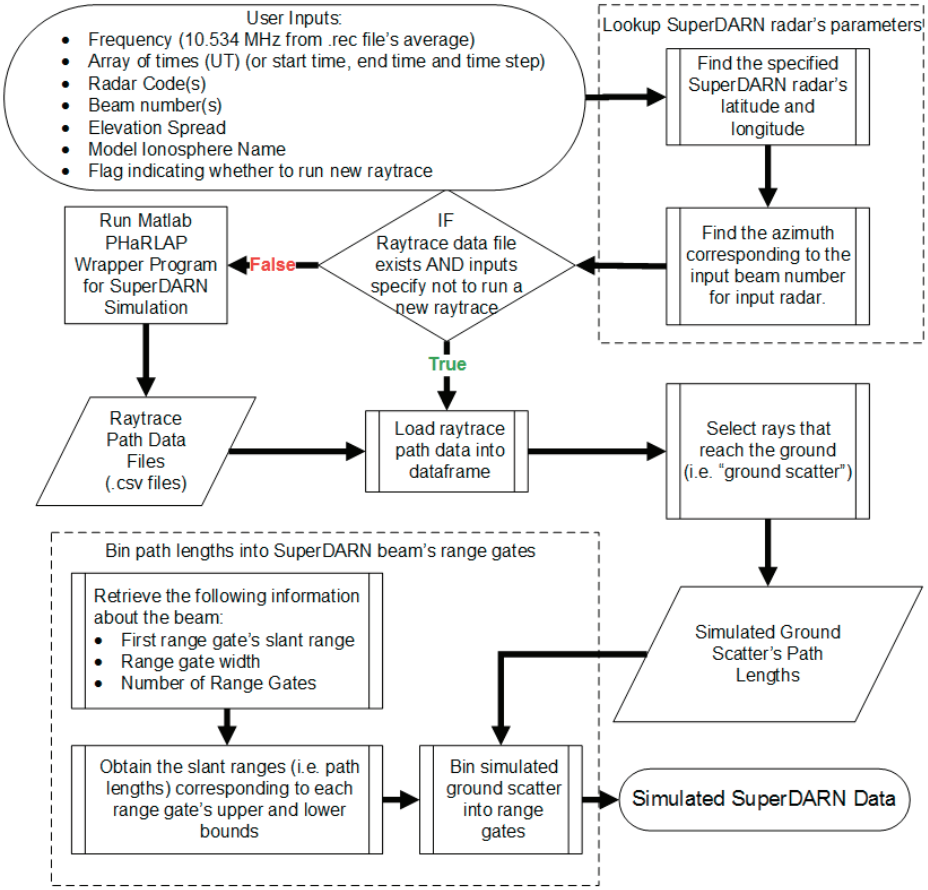

Figure 25. Flowchart of Python code that converts ray-trace path data into SuperDARN's data format.

4.1.4 Ray-Trace Data Visualization

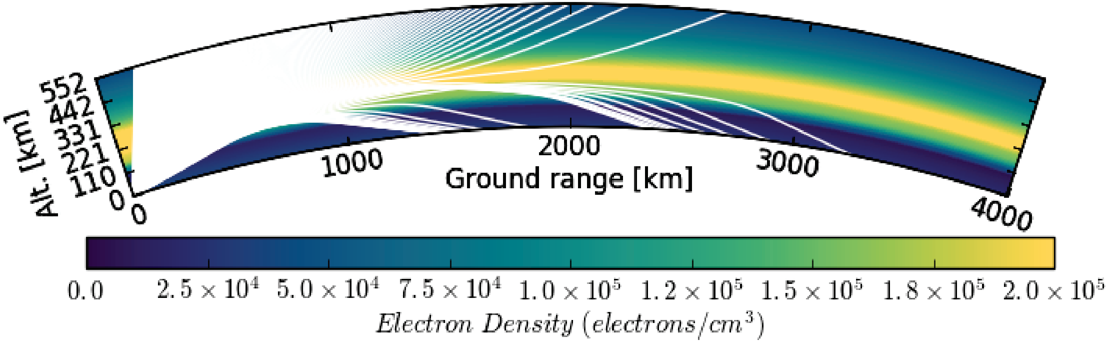

Figure 26. Example ray-trace profile plot for a ray-trace through the output of the unmodified SAMI2 model for CVE beam 0 (16.7°) at about 18:18 UT. The initial elevation of the rays goes from 10° to 70° in 0.25° steps.

The most common method of visualizing a ray-trace is a ray-trace profile plot, as shown in Figure 26. In a profile plot, ray paths are plotted over a colored background that shows the electron density or plasma frequency[4]. These plots are useful for examining ray propagation at a single time; however, the plots do not show the evolution of the paths over time, so they do not allow direct comparison to SuperDARN data.

In order to facilitate such comparisons, we generate a SuperDARN data object containing simulated data from the multiple ray-traces. These data are then plotted alongside measured SuperDARN data on RTI plots such as those shown in Figure 27. Our initial analysis utilizes only these two visualization methods.

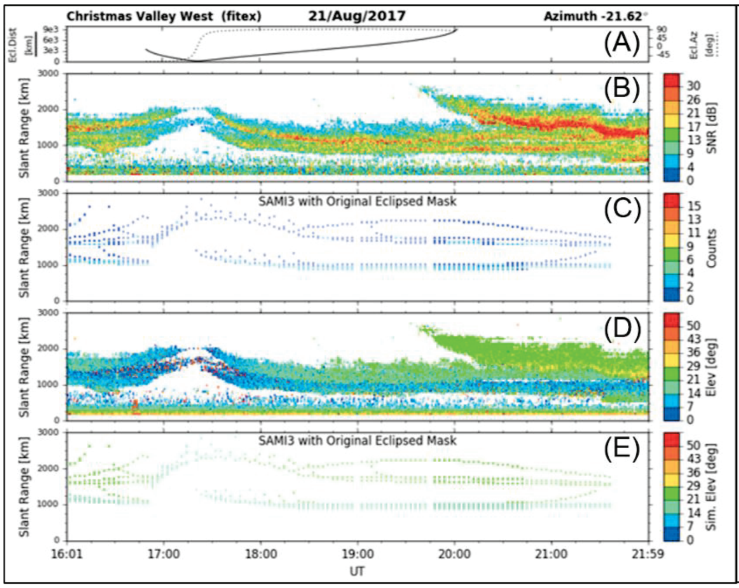

Panels of the RTI Comparison Plots:

A. Eclipse geometry panel:
   - Left: Distance (km) of the eclipse center from radar
   - Right: Azimuth (degrees) of the eclipse center, relative to direct north from radar

B. Measured Signal-to-Noise ratio (SNR) of received signals.

C. The number of simulated rays in each range gate.

D. Measured angle-of-arrival for returned scatter.

E. Simulated initial elevation angle of ground scattered rays, assumed to be equivalent to angle-of-arrival.

Figure 27. Example RTI comparison plot (left) of measured SNR and elevation angle data with simulated output data from original SAMI3 eclipse model. A description of each of the panels (by label) is given in the box on the right.

---

[4] Plasma frequency (f_p in MHz) is related to electron density (N in cm^{-3}) by $f_p \approx 9x10^{-3}\sqrt{N}$.

4.2 Initial Modeling Study with SAMI3

4.2.1 Initial SAMI3 Model

Prior to the eclipse, our research collaborators at NRL provided us with the output created by imposing their preliminary eclipse mask on the EUV input to SAMI3, as described in (Huba and Drob 2017). The initial modeling study preformed after the eclipse involved improving the eclipse masking function imposed on SAMI3, and determining the mechanism that leads to the increase in measured path lengths during the eclipse.

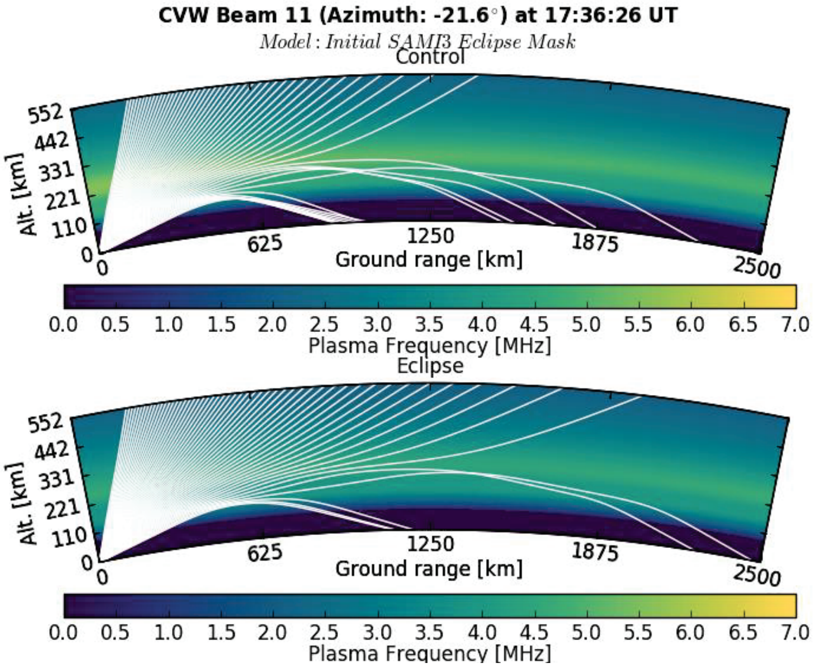

Figure 28. Comparison of ray-traces through uneclipsed (top plot) and eclipsed (bottom plot) SAMI3 models. The initial elevation angles of the rays are 15°-70° in 1° steps.

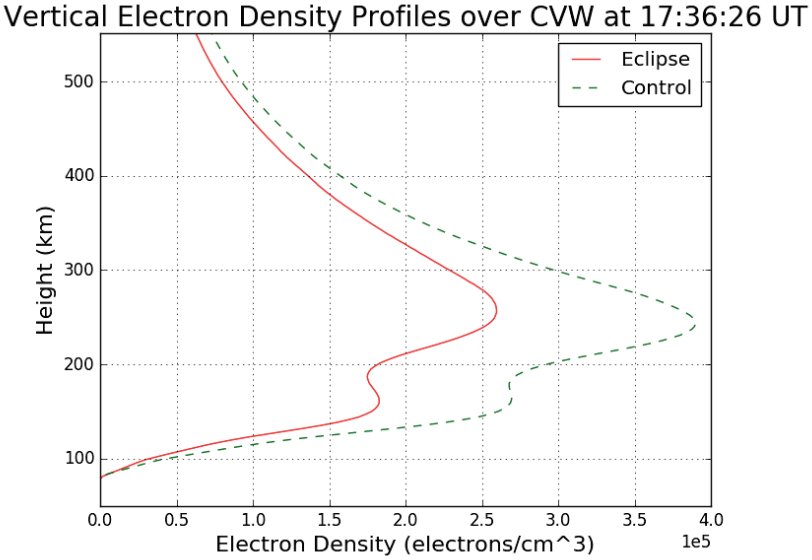

Figure 29. Electron density profiles over CVW from the uneclipsed (green) and eclipsed (red) SAMI3 models around the time of maximum eclipse magnitude at CVW.

The ray-traces through the output of the uneclipsed (control) SAMI3 model and the output of the eclipsed SAMI3 model are shown in the plots of Figure 28. These plots show that the rays that return to Earth in the eclipse case travel to farther ranges than the same rays did in the control case. Additionally, these rays that return to Earth in the eclipse case have lower take-off angles and appear to be refracted from slightly higher altitudes than the altitudes that rays with the same take-off angles were refracted from in the control case. However, as illustrated in the eclipsed and uneclipsed model vertical electron density profiles of Figure 29, the altitude of the peak electron density is approximately the same in both the eclipsed and uneclipsed models of Figure 28. Therefore, the ray-trace through the model ionosphere showed that the increase in slant range observed by SuperDARN is consistent with ducting of the signal through the eclipsed region instead of a change in ionospheric layer height.

Additionally, Figure 28 shows that the unperturbed ionosphere refracts more rays back toward the Earth than does the eclipsed ionosphere, and that both E and F region modes support longer ray paths during eclipsed conditions. Both of these effects are related to the lower plasma frequencies during the eclipse, which reduces the refractive angles by Snell's law:

$$n_0 sin\theta_0 = n_1 sin\theta_1 \tag{25}$$

where n_o and n_1 are the refractive indices of two different, adjacent media and θ_0 and θ_1 are the incidence angles of the ray measured relative to the normal of the interface between n_0 and n_1 in medium 0 and medium 1, respectively. Since the neutral atmosphere has an index of refraction of unity that does not vary during the eclipse, we can apply equation (25) to the eclipsed and uneclipsed case at this interface and obtain

$$n_u sin\theta_u = n_e sin\theta_e \tag{26}$$

where subscripts u and e denote the value of the given variable under uneclipsed and eclipsed conditions, respectively. The index of refraction is related to the plasma frequency of the ionosphere (ω_p) and the frequency of the ray (ω) by

$$n = \sqrt{1 - \frac{\omega_p^2}{\omega^2}} \tag{27}$$

(Hargreaves 1992). Since we know that the eclipsed ionospheric plasma frequency is less than the uneclipsed ionospheric plasma frequency, the index of refraction will be greater during the eclipse than under normal conditions for the same radio frequency. Hence the angle of refraction during the eclipse will decrease relative to uneclipsed conditions. Therefore, more rays at a given frequency will escape the eclipsed ionosphere than would escape under normal conditions.

4.2.2 Eclipse Mask Improvement

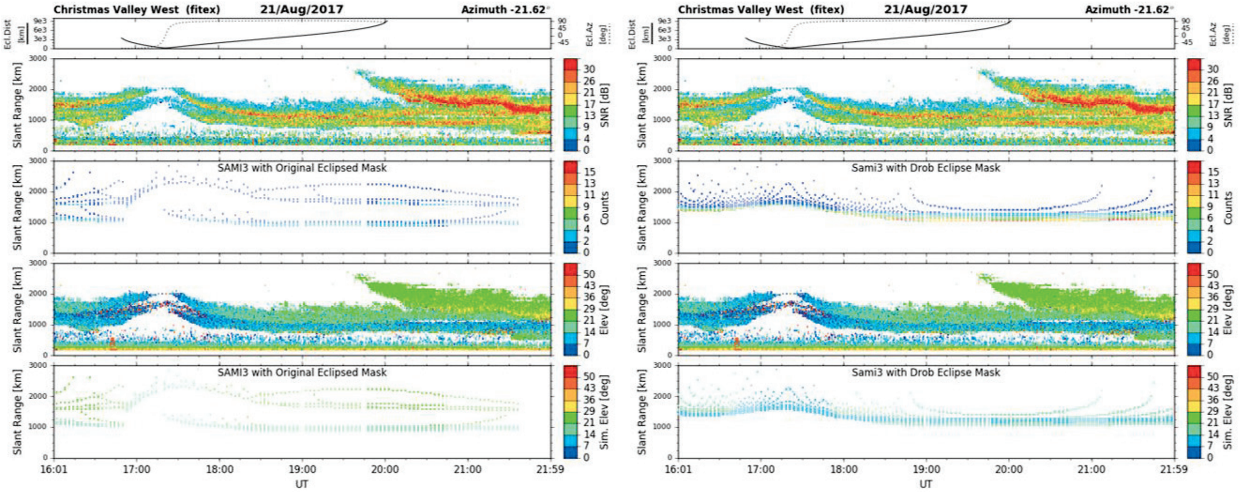

Figure 30. Comparison between these data generated by imposing the original eclipse mask on SAMI3 (left figure) and these data generated by imposing the Drob eclipse mask on SAMI3 (right figure).

The eclipse EUV mask discussed in (Huba and Drob 2017) was calculated over time at ground level; however, at ionospheric heights the eclipse was offset slightly from the ground-level times. This time delay is barely noticeable at Fort Hays, where the eclipse occurred around noon; however, it is significant at Christmas Valley, where the eclipse occurred in the morning. In order to correct for this time offset, the ray-trace output for CVW was shifted backwards in time by the time delay between the onset of eclipse at the midpoint of each ray's path and the onset of the eclipse at ground level[5]. Once this time correction was applied, time of the beginning of the eclipse onset period in the simulated data, marked by an increase in slant range of these data, closely matched that of these measured data from CVW as shown in the left plot of Figure 30.

As shown in the left plot of Figure 30, although the timescales of the ionospheric response during the eclipse onset are fairly well represented by the model, there are significant differences between these measured and modeled data in the recovery period. These problems include:

- the simulated elevation angles are significantly higher than measured ones
- a significant asymmetry exists in the onset and recovery phases of the simulated data
- the simulations have long recovery periods relative to these measured data

The first step in addressing these issues was to develop a more accurate eclipse masking function. Collaborators at NRL along with VT developed such an improved masking function after the eclipse, called the "Drob eclipse mask". The Drob model of the eclipse calculates the eclipse mask as a function of latitude, longitude, altitude, and time (Hairston, Mrak et al. 2018). As the right plot of Figure 30 shows, imposing the

---

[5] The times given in the titles of Figure 28 and Figure 29 are the "corrected times" given by this method

Drob eclipse mask on the input EUV to SAMI3 produces simulated data with elevation angles very close to the measured values, and timescales much closer to those of the measured eclipse response. It should be noted that the ray-trace through the output of the original masked SAMI3 model was only run for elevations 15°-70° in 1° steps, whereas the ray-trace through the output of the Drob masked SAMI3 model was run for elevations 10°-50° in 0.25° steps. The elevation angle spread had to be changed for ray-tracing through the Drob model as ray-tracing through the Drob model using the original elevation spread returned almost no scatter.

The Drob mask appears to more accurately represent the eclipse obscuration, since its data agree with both the measured data timescales and the elevation angles that led to good echoes. However, the recovery period of these “Drob model” simulated data is still significantly longer than that of these measured data. Hence, the Drob mask produces simulated data that are much closer to the measured data, but some phenomena associated with ionospheric eclipse dynamics are not correctly accounted for in the SAMI model.

4.3 Model Results and Further Questions

These initial modeling studies prove that the observed increase in slant range of the returned scatter observed by the SuperDARN system is likely due to ducting through the depleted, eclipsed ionosphere, rather than changes in the heights of the ionospheric layers during the eclipse. Additionally, these ray-trace simulations have helped to refine our EUV eclipse mask by comparison with measured data. Finally, these comparisons have also indicated that our one-hop assumption is reasonable, because the simulated one-hop path lengths are comparable to the measured slant ranges. However, as discussed in section 4.2.2, some features of the eclipse response are not captured in the current eclipsed SAMI3 model. There are several phenomena that might be responsible for this, such as perturbation electric fields induced in the vicinity of the eclipse, enhanced diffusion along the flux tubes, or prevailing neutral winds at the local times of the eclipse at each site. SAMI uses default Horizontal-Wind-Model[6] (HWM) values for the thermospheric neutral winds (henceforth referred to as “neutral winds”), the eclipsed neutral wind velocity may not be accurately represented in the model. The investigation of if and/or how changes in the neutral wind velocity may affect the SuperDARN ray-trace simulation is the focus of the next chapter.

---

[6] HWM is an empirical model, where values are determined from statistical fits to measured data.

Chapter 5

5.1 Motivation for Neutral Wind Effect Study

As discussed in Chapter 4, by default SAMI uses the HWM empirical model of thermospheric winds to set the initial neutral wind velocities (Huba, Joyce et al. 2000). However, since HWM is based on the statistical averages of many observations, it may not give accurate values during such a rare event as an eclipse. Furthermore, since gravity waves and other motions have been observed to be created by eclipses (Stankov, Bergeot et al. 2017), the local neutral wind is likely to be different from the average wind given by the model. Unfortunately, no neutral wind measurements during the eclipse are available at CV or FH. Hence the only way to obtain an approximation of the eclipsed neutral wind velocity is through modeling. Validation of these neutral wind models can be performed by imposing neutral winds in SAMI3, raytracing through its output, and comparing these simulated data to measured SuperDARN data. Since SAMI3 is computationally intensive, it would be time consuming to run multiple case studies in order to determine which case best fits these measured eclipse data. This process can be expedited by running case studies in SAMI2 to evaluate the relative impacts of different neutral winds on the ray-trace output. This allows us to compare particular winds to their modeled effects, which develops intuition and allows particular plasma effects to be better understood. The goal of the study presented here is to take an initial step toward evaluating the impact of various neutral winds imposed in SAMI2 on the simulated SuperDARN data.

5.2 Neutral Wind Study Methodology

5.2.1 Neutral Wind Cases

Custom neutral wind velocities were input to SAMI2 and run for different times for both eclipsed (Drob eclipse mask) and uneclipsed (control) ionospheres. The four neutral wind cases presented are: 1) default wind values from HWM, 2) no wind, 3) north/south wind values from HWM with no east/west wind, and 4) east/west wind values from HWM with no north/south wind. For reference, the horizontal neutral wind velocities from HWM at each site for the eclipse day are given in Figure 31. The red and blue vectors in Figure 31 show the wind vectors given by the HWM model at each point. The right plot gives the horizontal wind vectors at various ranges along the radar beam and altitudes from each radar site, and the left plot gives the horizontal wind vectors at each radar site for various altitudes as a function of time. Eastward winds correspond to vectors pointing to the right and northward winds correspond to vectors pointing toward the top of the pages. The HWM wind speed is greater at CV than at FH over the course of the day as shown in the left plot. However, at ranges further from each radars at 18 UT, the HWM wind speed along FHW beam 19 and CVE beam 0 are almost equal at long ranges. Additionally, at F region altitudes the HWM wind direction at both sites is towards the north-west throughout the entire time period of interest.

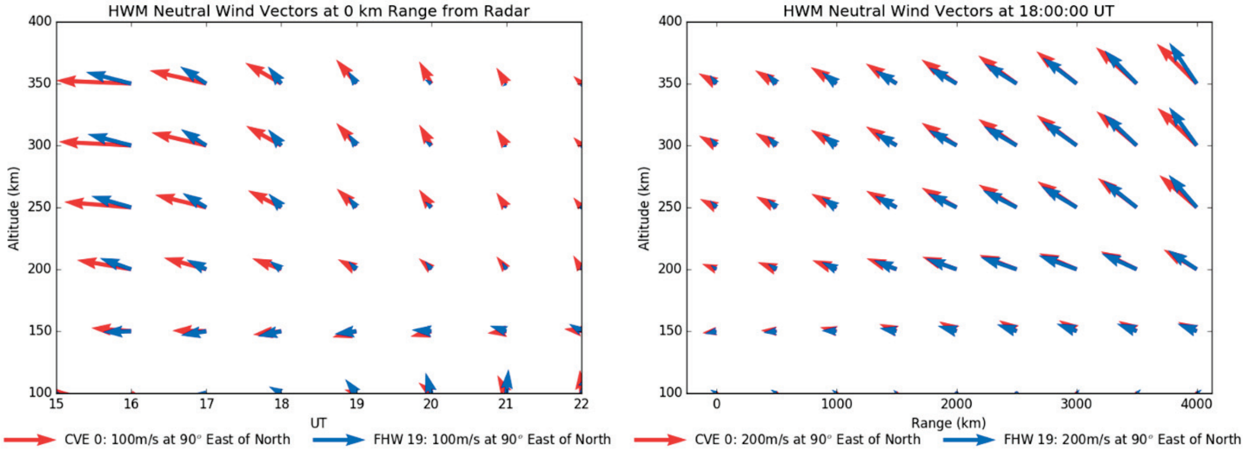

Figure 31. HWM neutral wind vectors (north is positive y and east is positive x) over altitude vs. range (left plot) and altitude vs. time (right plot).

5.2.2 Ray-trace Conditions and Visualization

SAMI2 calculates the plasma density along a magnetic flux tube, so the simulated SuperDARN beam must be as closely aligned with the local magnetic declination as possible for accurate results (*i.e.* the beam azimuth should be almost equal to the declination angle of the local magnetic field). Additionally, in order to compare ray-trace outputs with measured data, the particular azimuth selected for study at each site must also have data from eclipse day. The beams that best fulfill these criteria are given in Table 5.

Site	Magnetic Declination	Best Aligned Beam	Azimuth
Christmas Valley	~14.3^{o}	CVE beam 0	16.74^{o}
Fort Hays	~4.8^{o}	FHW beam 19	2.54^{o}

Table 5. For each SuperDARN site, the magnetic declination angle and the beam with data that best aligns with it.

In order to evaluate the temporal evolution of the ray-trace profiles, a custom line-plot visualization scheme was created. As illustrated in Figure 32, for each simulated time the path lengths (or slant ranges) of all rays that returned to Earth within the preset range bounds were averaged together to obtain the mean path length of the simulated ground scatter. These averages are plotted as dots in the figure for both the control day (green) and the eclipse day (red). The minimum and maximum path lengths that returned to ground are plotted as vertical bars through these points. Thus, the average path lengths are plotted over time with their range indicated by the vertical bars through each point. This process is performed for both eclipse and control (uneclipsed) SAMI2 models, each with the same neutral wind velocity. This plot format is used in the sections that follow to identify the effects of different hypothetical wind fields on the radar data.

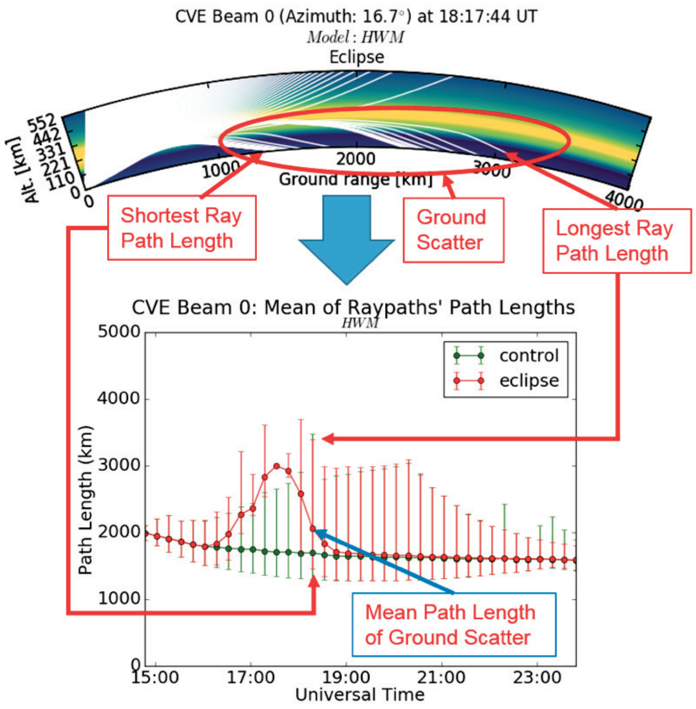

Figure 32. Process for converting eclipse case raytrace data from a profile visualization to a line-plot visualization.

5.3 Results and Analysis

5.3.1 SAMI2 Ray-trace Results

The line-plots from ray-traces through the output of SAMI2 for each of the four neutral wind cases are shown above for CV (Figure 33) and FH (Figure 34). At each site, these control data vary only slightly between different wind cases. However, the eclipse data vary substantially with neutral wind, and are also quite different at the two radar sites.

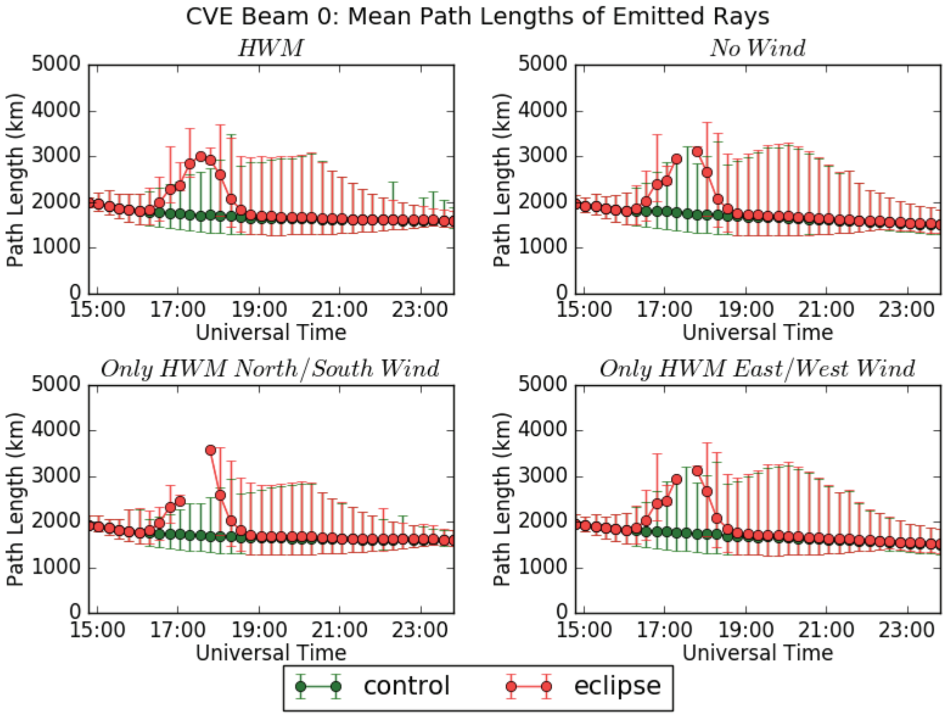

Figure 33. Line-plots from ray-trace through output of SAMI2 models initialized with four different wind models at Christmas Valley.

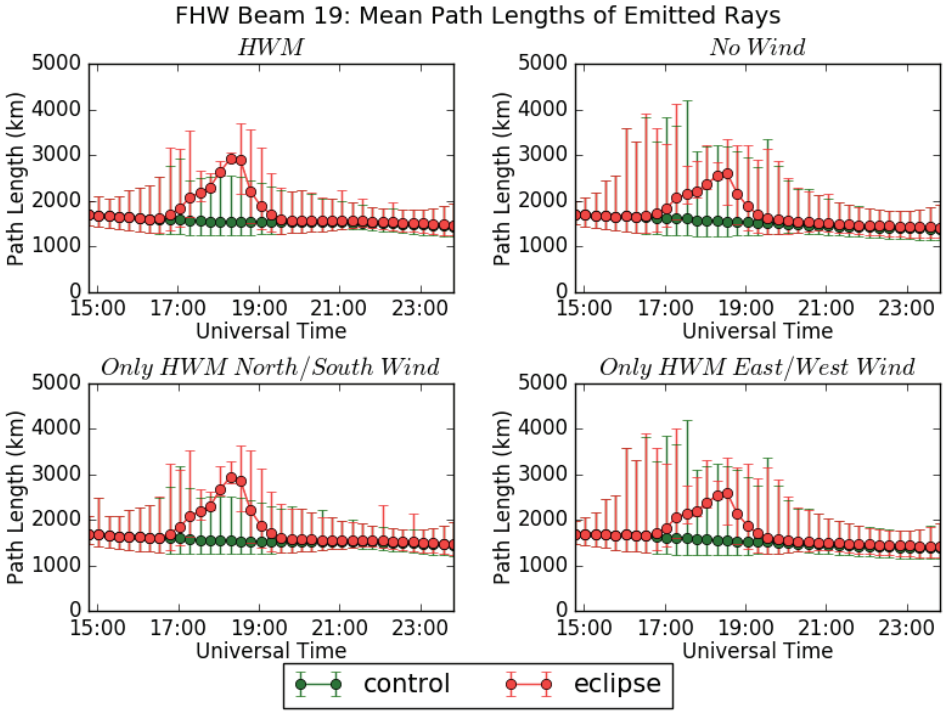

Figure 34. Line-plots from ray-trace through output of SAMI2 models initialized with four different wind models at Fort Hays.

During the eclipse period at each site and in all wind cases, the path length of the rays increases while the number of rays that return to the ground decreases. This is indicated by the narrowing of the vertical bars in the ray-trace profiles. In each wind case at CVE, except for “HWM", there is a period around eclipse maximum where no rays return to the ground. In contrast, for every wind case at FHW one or more rays reach the ground at every modeled time, even during maximum eclipse. Another difference between the two sites is that during eclipse onset the maximum path lengths at FHW, in most wind cases, are greater than those of CVE during eclipse onset. In contrast, during the recovery phase and post-eclipse, the spread of paths lengths is usually greater at CVE than at FHW.

When comparing the eclipse plots of different wind cases at a site, another feature of note is that at each site the “Only HWM East/West Wind” plot is almost identical to the “No Wind” plot. In contrast, the “Only HWM North/South Wind” plot at each site differs significantly from the “No Wind” plot. This suggests that the zonal (eastward) wind does not have as much of an impact on the model plasma densities as the meridional (northward) wind does. However, the zonal wind does appear to have some effect on the ionospheric eclipse response at CVE, because the “Only HWM North/South Wind” plot differs significantly from the “HWM” plot. In the former case there is a short interval in which all the rays escape near the maximum eclipse phase, whereas in the “HWM” plot there is always at least one ray that returns to the ground. In contrast, there is almost no difference between FHW’s “HWM” and “Only HWM North/South Wind” eclipse plots, suggesting that the zonal wind plays almost no role in the ionospheric eclipse response at FHW.

Overall, at both sites, variations in the meridional neutral wind velocity produce larger eclipse deviations compared to the “No Wind” case than do variations in the zonal neutral wind. This supports the conclusion that the meridional winds have a greater impact on the eclipsed ionosphere than do the zonal winds. The zonal wind appears to have a small impact on the eclipse response at CVE, but almost no impact on the eclipse response at FHW. In order to explain these phenomena, the neutral wind-induced plasma drift equations must be examined.

5.3.2 Analytical Analysis of Neutral Wind-Induced Drift Velocity

The general form of the neutral-wind induced plasma drift velocity was presented in section 2.2.3.3. The derivation of the neutral-wind induced charged particle drift velocity begins with the equation below for the net force exerted on a particle of species j by (1) the local magnetic field via the Lorentz Force; (2) the neutral wind; and (3) ion-neutral collisions. Modification of Equation (11) from section 2.2.3 leads to

$$\vec{\mathrm{F}}_{\mathrm{j,net}} = \mathrm{m_j n_j}\frac{\mathrm{d}\vec{\mathrm{v}}_\mathrm{j}}{\mathrm{dt}} = \underset{(1)}{\mathrm{n_j q_j}\left(\vec{\mathrm{v}}_\mathrm{j}\mathrm{x}\vec{\mathrm{B}}\right)} + \underset{(2)}{\mathrm{n_j m_j}\nu_\mathrm{j}\vec{\mathrm{U}}} - \underset{(3)}{\mathrm{n_j m_j}\nu_\mathrm{j}\vec{\mathrm{v}}_\mathrm{j}} \tag{28}$$

where the electric field and pressure gradient terms have been dropped in order to focus on just the effects due to the neutral wind, and the symbols are defined as:

n_j : Number density of species j
q_j : Charge of species j
$\vec{v}_j$: Neutral wind-induced drift velocity of species j
$\vec{B}$: Magnetic flux density
ν_j : Species j ion-neutral collision frequency
$\vec{U}$: Neutral wind velocity

Under steady-state conditions $\vec{F}_{j,net} = 0$ and Equation (28) becomes

$$m_j \nu_j \vec{v}_j = q_j\left(\vec{v}_j x \vec{B}\right) + m_j \nu_j \vec{U} \quad (29)$$

Solving for the drift velocity yields

$$\vec{v}_j = \underset{\text{(Direct)}}{\frac{\nu_j^2}{\omega_j^2 + \nu_j^2}\vec{U}} + \underset{\text{(Parallel)}}{\frac{\omega_j^2}{\omega_j^2 + \nu_j^2}\frac{\left(\vec{U} \cdot \vec{B}\right)\vec{B}}{\left|\vec{B}\right|^2}} + \underset{\text{(Perpendicular)}}{\frac{\nu_j \omega_j}{\omega_j^2 + \nu_j^2}\frac{\vec{U} \times \vec{B}}{\left|\vec{B}\right|}} \quad (30)$$

where ω_j is the gyrofrequency of species j. As shown in equation (30), the wind-induced charged particle drift velocity depends on three components: the Direct component, the Parallel component and the Perpendicular component (Rishbeth and Garriott 1969). These are characterized by the direction of their velocity relative to $\vec{U}$ and $\vec{B}$, as shown in Table 6.

Component	**Velocity Direction**
Direct	Parallel to $\vec{U}$
Parallel	Parallel to $\vec{B}$
Perpendicular	Perpendicular to both $\vec{U}$ and $\vec{B}$

Table 6. Description of neutral wind-induced drift velocity components.

The relative magnitudes of each component vary with gyrofrequency and ion-neutral collision frequency, both of which are altitude dependent. For this reason the contribution of each component in equation (30) varies with altitude as well as species. As shown in Figure 35, at F region altitudes (above about 150km) the Perpendicular and Direct components are negligible compared to the Parallel component. Therefore, the component of the wind that is most closely aligned to the magnetic field will have the greatest impact on the wind-induced drift velocity at high altitudes. Since the geomagnetic field generally has its largest component in the north-south-zenith-nadir plane, one would expect the east-west (zonal) component of the wind to have less effect on plasma motions than the north-south (meridional) component. Note that vertically directed winds would also be very important, but it is well known that the horizontal components of the thermospheric wind are generally much larger than the vertical winds, so this component can generally be neglected.

At low altitudes there is a thin region in which the Perpendicular component dominates, while below this region the Direct component is most significant. Since our focus in on the refraction of rays that reach high altitudes, and therefore have long ray paths, the lower altitude effects are relatively unimportant. Additionally, as most rays appear to have an apogee around or above 150km, the effects below about 150km are not relevant to our main focus here.

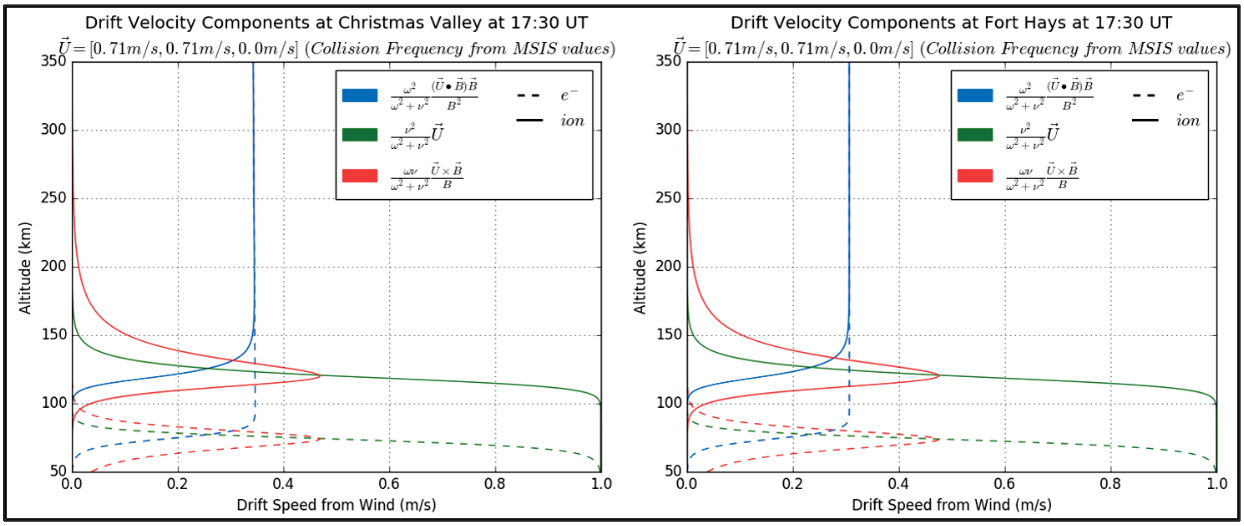

Figure 35. Magnitude of the wind-induced drift velocity's three components with a driving neutral wind with a magnitude of 1m/s at 45^o East of North.

The horizontal component of the magnetic fields at the CV and FH SuperDARN sites differ from one another as illustrated in Figure 36. The vertical component of the magnetic field is almost the same at each site, with dip angles of about 66.125^o at CV and dip angles of about 66.309^o at FH. Thus, the ionosphere will respond differently at each site in response to the same neutral wind, as shown in Figure 37[7]. The figure indicates that the plasma drift velocity at FH does not change quite as much as that at CV for the same change in the zonal wind magnitude. This explains why the “Only North/South HWM Wind” and the “HWM” cases appeared more similar in the FH simulation than in the CV simulation. Additionally, Figure 37 indicates that the theoretical plasma drift velocity at both CV and FH is more strongly driven by the meridional wind than by a zonal wind. Thus, due to the magnetic field orientation at these SuperDARN sites, the meridional wind is expected to have a greater impact on the wind-induced plasma drift velocity than the zonal wind, especially at FH where the declination is smaller. Note that vertical plasma motion is also driven at high altitudes by meridional winds, because the mobility of the charged particles is greatest parallel to B. For example a northward wind will move plasma downwards within a flux tube in the northern hemisphere due to the Parallel component of the ion drift.

---

[7] Wind-induced drift velocities were calculated from equation (30) using collision frequency values from MSIS and the mean ion mass and collision frequency.

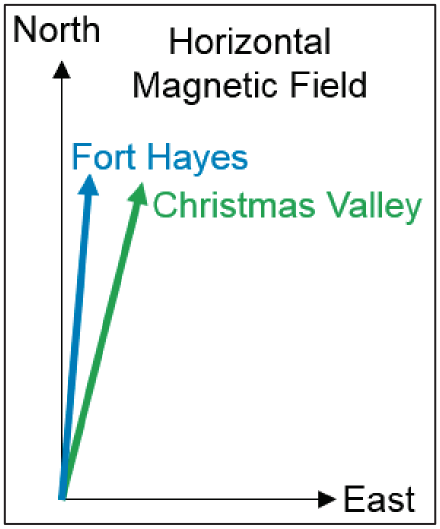

Figure 36. Horizontal magnetic field orientation at each SuperDARN site.

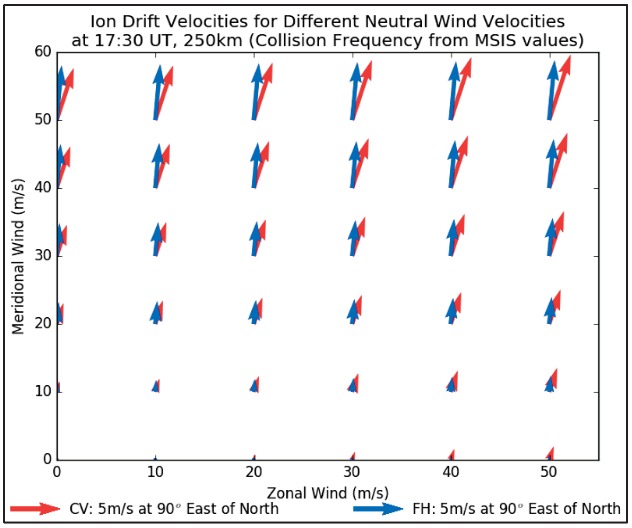

Figure 37. Ion drift velocities at 250km resulting from different zonal (x-axis) and meridional (y-axis) wind speeds. (The electron drift velocity plot is almost identical at this altitude.)

5.3.3 Comparison to SuperDARN Data

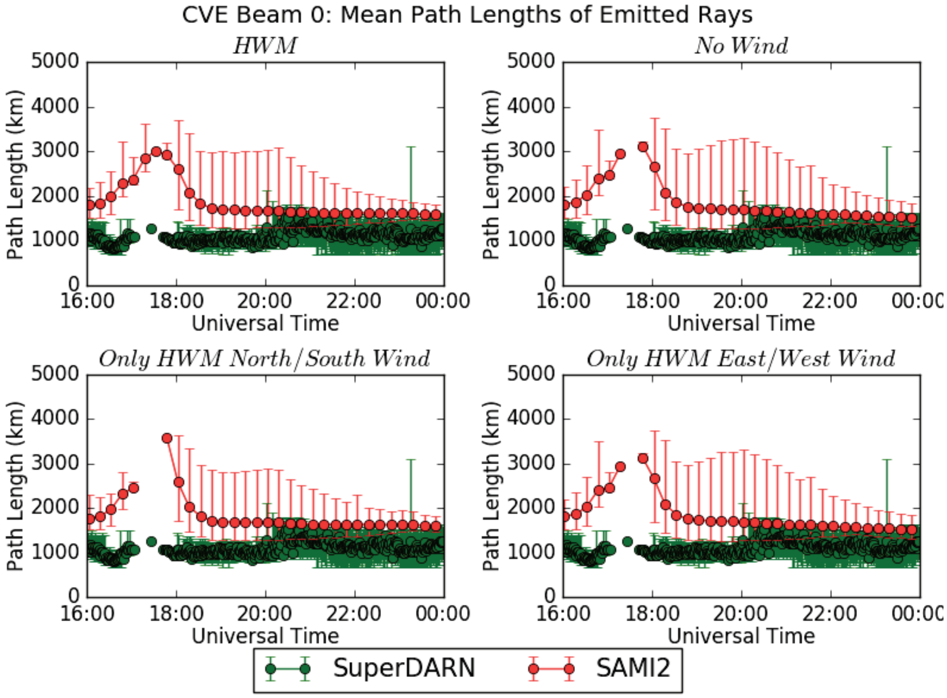

Figure 38. Line-plots comparing wind study eclipse simulations to measured CVE slant range data (past range gate 10).

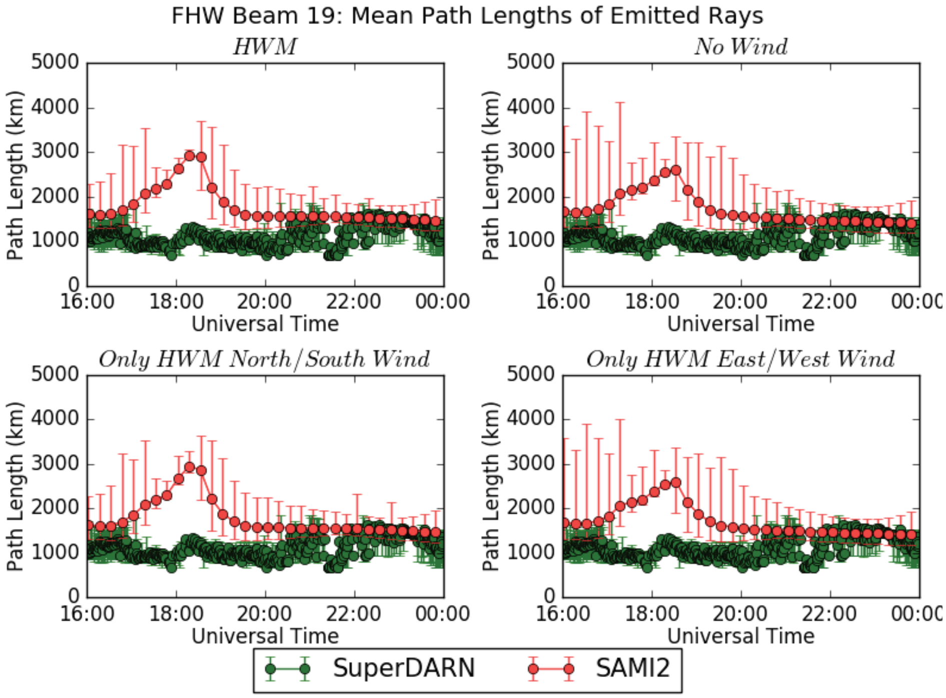

Figure 39. Line-plots comparing wind study eclipse simulations to measured FHW slant range data (past range gate 10).

A comparison between the ray-trace outputs from the model wind study and the measured SuperDARN data is presented in Figure 38 and Figure 39. The green dots and vertical lines show the SuperDARN data, and are the same for all four plots at each site. The red dots and vertical lines show the simulated data. Significantly, the measured data from CV show a loss of signal around the time of totality, which is similar to that of the "Only HWM North/South Wind" case. Neither the measured nor the simulated data at FH experienced a total signal loss around totality. Additionally, none of these FHW simulated data appear to follow the trends of these measured data at eclipse onset. More rigorous models of the neutral wind velocity might improve some of these inconsistencies; however, this is outside the scope of the work presented here and, hence, is left for future studies. Figure 38 and Figure 39 do not show good agreement between the simulated and measured data at either site during the eclipse, regardless of the wind. This suggests that either the HWM wind does not correctly capture winds during the eclipse, or that other factors such as electric fields and pressure gradients are more important than winds in driving plasma motions during eclipses. Additional modeling studies may help to resolve this issue.

5.4 Summary

This neutral wind study indicates that the wind direction is capable of changing the observed ionospheric response to the eclipse. Ray-traces through the output of various SAMI2 cases indicate that the mid-latitude ionosphere is particularly sensitive to changes in the meridional winds. Examination of the equation for neutral wind-induced plasma drift velocity reveals that at F region altitudes, where the ionospheric plasma density is largest during the eclipse, the neutral wind-induced drift velocity is primarily driven by the magnetic field-aligned component of the neutral wind velocity. Hence, as the magnetic declination angle decreases, changes in the meridional wind have more of an impact on the wind-induced drift velocity while changes in the zonal wind have less impact. Since the declination of the magnetic field at each of the SuperDARN sites considered here is small, the meridional wind is more aligned with the magnetic field than the zonal wind and hence has more of an impact on the ionosphere. Additionally, since the declination is somewhat smaller at FH than at CV, the zonal wind has less of an effect on the ionosphere at FH than it does at CV. The Parallel component of the wind-driven ion drift is also important to the vertical ion drift, but the diffusive drift due to the flux-tube aligned pressure gradient may dominate the wind-driven ion drift. Finally, the studies shown here demonstrate that the combination of SAMI3 modeling and raytracing is a useful approach for examining the wealth of factors that affect the F region plasma during eclipses. We describe some ideas for further studies in the next chapter.

Chapter 6

6.1 Summary

The dominant effects of the 2017 eclipse on the SuperDARN radars data at CV and FH were an increase in slant range and a decrease in the number of rays that were refracted back toward the Earth relative to pre-eclipse observations. The latter statement implies that the total amount of transmitted radar power escaping into space increases when the rays travel through the eclipsed F region. There is also an azimuthal asymmetry - the measured magnitude of the eclipse response appears to decrease as the radar looks away from the west and towards the east. Additonally, the CV radars observed decreases in angles-of-arrival (elevation angles) of returned scatter during the eclipse. The low velocities and small spectral widths of these SuperDARN data indicate that the majority of observed scatter is ground scatter. The ray-trace model simulates SuperDARN ground scatter, and the dominance of ground scatter in these SuperDARN measurements strengthens the comparisons between these data and our models. Aditionally, the existence of elevation angle data at CVE and CVW allows for additional validation of the performance of the models.

Our model ionospheric density profiles are generated by imposing an eclipse mask on the EUV input to the SAMI numerical model. A ray-trace simulation of SuperDARN is then run through these output ionospheric profiles in order to generate simulated SuperDARN ground scatter data. Comparison of the simulated timescales and elevations (for CV radars) with those of measured data allows us to evaluate the accuracy of our SAMI models and the EUV mask. Our work shows that this is a useful technique for studying how various forcing terms (herein limited to winds) can affect the radar data during eclipses.

Using these methods we have performed several initial studies: 1) an investigation of the nature of the increase in slant range during the eclipse; 2) a validation of an improved imposed on SAMI; and 3) a study of the impact of neutral wind direction on eclipse dynamics. Our ray-trace profiles through the eclipsed SAMI3 output indicate that rays were ducted through the depleted plasma in the eclipsed region. Thus, the observed increase in slant range is likely due to ducting of rays through the eclipsed region instead of a change in layer altitude. However, the initial eclipse mask imposed on SAMI3 produces simulated data with much longer recovery times and higher elevation angles than that observed by SuperDARN. An improved eclipse mask that increases the resolution of the obscuration as a function of latitude, longitude, altitude and time produces better agreement between the simulated and measured data; however, the modeled recovery time is still too long. This indicates that further improvements to the SAMI model are necessary to correctly model eclipse dynamics. In order to investigate one such case we performed a neutral wind study using the SAMI and PHaRLAP algorithms. The major result of this study is the finding that the meridional neutral winds have a greater impact on the ionospheric eclipse response than do the zonal neutral winds. Since neutral winds are very difficult to measure, the models of their behavior are not as mature as the IRI and MSIS models, especially during unusual phenomena like eclipses. Thus our study highlights a new reason for improving thermospheric wind models and measurements.

6.2 Conclusions

This study has produced several ray-trace tools for evaluating SAMI2 and SAMI3 models. Using these tools, we have determined that the increased slant range observed by the SuperDARN radars during the eclipse is likely due to ducting of radio waves through the depleted plasma of the eclipsed region. The four-dimensional accurate scaling of the EUV flux in SAMI3 produced by the improved Drob mask produces output ray-trace data that agree more closely with these observed data in elevation and onset time of eclipse-induced ionospheric effects. However, the recovery time period of the simulation disagrees sharply with observations, so some parameter(s) of the eclipse model is/are inaccurate. One likely candidate is the neutral wind velocity during the eclipse, so we investigated the effect of the neutral wind on our SuperDARN simulation using SAMI2. The results indicate that the ionosphere is more sensitive to changes in meridional wind than to changes in zonal wind because of the magnetic field declination at the latitudes of interest. This importance of wind direction to the ionospheric eclipse response that is demonstrated by this work will help guide future development of eclipse wind models.

6.3 Future Work

6.3.1 Modeling the 2017 Eclipse

Evaluation of additional neutral wind models will likely be the subject of future work. Implementation of promising neutral wind models into SAMI3 will allow for model-to-measurement comparisons along all SuperDARN look directions that show data modified by the eclipse. These comparisons might shed light on why the observed eclipse response varies with look-direction and radar site.

Additionally, there are other phenomena that SAMI may not capture with sufficient accuracy to model plasma motion during the eclipse. For instance, parallel and perpendicular plasma diffusion effects (described in section 2.2.3.1) are likely to have a significant effect on the ionospheric eclipse recovery. Local electric fields associated with the plasma density gradients created by the eclipse would also drive plasma transport, primarily perpendicular to the magnetic field. A future ray-trace simulation study could investigate all of these effects and could potentially lead to modifications that would help to correct the recovery phase differences between models and measurements.

6.3.2 Study of the 2024 Eclipse

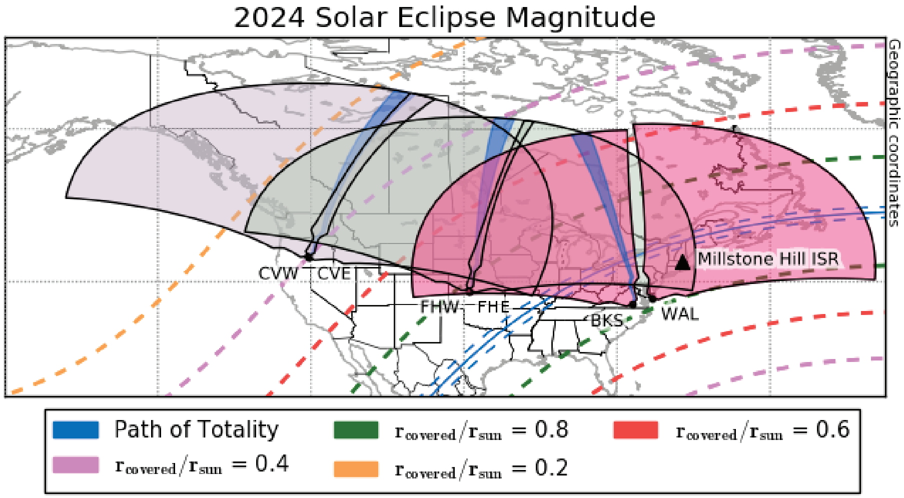

Figure 40. The umbra and penumbra of the 2024 eclipse in relation to SuperDARN radars (violet, green and pink) and the Millstone Hill ISR (black triangle). SuperDARN beams closely aligned with the magnetic field are highlighted in indigo. (Eclipse path data from (Jubier 2005).)

The next CONUS eclipse on April 8, 2024 will have a south-to-north track, as shown in Figure 40. The path of totality will cross the FHE and Blackstone[8] (BKS) SuperDARN Fields of View as well as that of the Wallops (WAL) SuperDARN radar, which may be operational by that time. Additionally, as Figure 40 shows, all of the active US SuperDARN radars will be at least partially encompassed in the eclipse penumbra. The every-other-beam mode was a useful operating mode during the 2017 eclipse. A similar operating mode should be employed for SuperDARN radars during the 2024 eclipse, but with some modifications. Specifically, the operating mode should include measurements from beams most closely aligned with the local magnetic field at each site, highlighted in indigo in Figure 40. Additionally, the radars should obtain control data by operating in eclipse-day mode for at least the day before the eclipse and the day after. This would provide a control data set for comparison that was not available in 2017 because the radars operated on a different frequency the days before and after the eclipse. Based on the work described herein, we recommend that the eclipse mode should be run for a period encompassing the time of the eclipse for several days before and after the eclipse day. Alternatively, the eclipse mode could be run continuously for 48-72 hours, starting at least one day before the eclipse.

The geometry of the 2024 eclipse path differs from that of the 2017 eclipse, as shown in Figure 40. The 2024 eclipse path will be more aligned with the magnetic field in the CONUS than that of 2017. Additionally, the eclipse will begin around noon over the CONUS. As shown in section 2.2.4, the geometry of the eclipse and solar zenith angle relative to the magnetic field has a great influence on the ionospheric eclipse response.

---

[8] BKS did not operate in the same mode as the CV and FH radars on eclipse day in 2017 as its FOV did not intersect the path of totality. Hence, it has been omitted from this study.

Other differences between these two eclipses include the time of year and the point in the solar cycle. In planning a study of the ionospheric response to the 2024 eclipse and interpreting its results, these differences should be taken into account as well as the lessons learned from the 2017 eclipse.

Finally, another resource that will be available during the 2024 eclipse is the Millstone Hill Incoherent Scatter Radar (ISR) in Massachusetts. The Millstone Hill ISR can infer the neutral wind velocity along the magnetic field from its backscatter measurements. It was operational during the 2017 eclipse, but it was not in the path of totality. However, in 2024 the path of totality will come much closer to Millstone and may be in the FOV of the ISR. Measurements that could be obtained include electron and ion temperatures, line-of-sight plasma velocities, electron density and estimates of ion composition (Hargreaves 1992). The field-aligned component of the neutral wind velocity and diffusion-driven drifts could be derived from these ISR measurements as well (Hargreaves 1992). The ISR could also perform altitude scans in a fixed azimuth to help separate the importance of diffusion, winds, and electric fields during the 2024 eclipse. These measurements, along with those from the SuperDARN radars, should be useful for seeding and evaluating improved models of the eclipsed ionosphere.

Appendix A: SuperDARN Radars' Operation

A.1 Eclipse Experiment Beam Azimuth Reference Tables for SuperDARN Radars

For each radar used in the eclipse experiment, a reference table provides a reference table for each operational beam of each SuperDARN radar used in the eclipse experiment.
Each section has a reference table for the azimuth of each beam with eclipse data

For each SuperDARN radar operational during the eclipse, a reference table for the azimuth of each beam with eclipse data is given.

A.1.1 Christmas Valley West Reference Table

Beam Number	**Azimuth (Degrees East of North)**	**Camping Beam**
3	-47.54°	No
5	-41.06°	No
7	-34.58°	No
9	-28.1°	No
11	-21.62°	Yes
13	-15.14°	No
15	-8.66°	No
17	-2.18°	No
19	4.3°	No
21	10.78°	No
23	17.26°	No

A.1.2 Christmas Valley East Reference Table

Beam Number	**Azimuth (Degrees East of North)**	**Camping Beam**
0	16.74°	No
2	23.22°	No
4	29.7°	No
6	36.18°	No
8	42.66°	No
10	49.14°	Yes
12	55.62°	No
14	62.1°	No
16	68.58°	No
18	75.06°	No
20	81.54°	No

A.1.3 Fort Hays West Reference Table

Beam Number	Azimuth (Degrees East of North)	Camping Beam
1	-55.78°	No
3	-49.3°	No
5	-42.82°	No
7	-36.34°	No
9	-29.86°	No
11	-23.38°	Yes
13	-16.9°	No
15	-10.42°	No
17	-3.92°	No
19	2.54°	No
21	9.02°	No

A.1.4 Fort Hays East Reference Table

Beam Number	Azimuth (Degrees East of North)	Camping Beam
0	10.98°	No
2	17.46°	No
4	23.94°	No
6	30.42°	No
8	36.9°	No
10	43.38°	Yes
12	49.86°	No
14	56.34°	No
16	62.82°	No
18	69.3°	No
20	75.78°	No

A.2 SuperDARN Radar Operation Summary

Parameter	Value
Operating Frequency (average)	~10.5 MHz
Time to Complete FOV Scan	1 minute
Non-Camping Beam Temporal Resolution	~ 1 minute
Camping Beam Temporal Resolution	~ 6 seconds
Number of Range Gates per Beam	100
Distance of First Range Gate from Radar	180 km
Width of each Range Gate	45 km

Appendix B: SuperDARN Ray-trace Simulation

B.1 Overview

An overview of the SuperDARN ray-trace simulation was given in section 4.1.3. Appendix B provides more details on the relevant codes and programs used in this simulation as a guide for its future use. As shown in Figure 41, there are two main blocks of code that are intertwined the MATLAB Ray-trace function and the Python rayBeamObj. These are described in the following two sections.

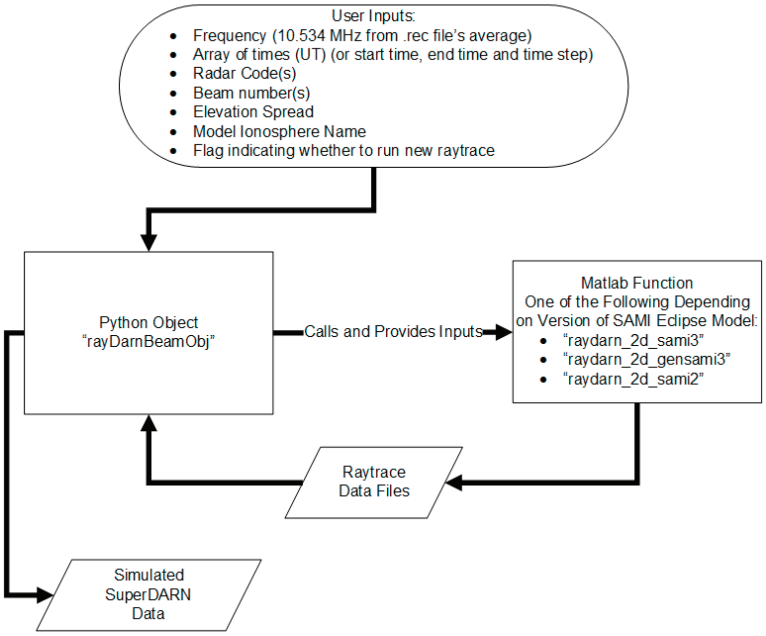

Figure 41. Overview of SuperDARN Simulation

B.2 MATLAB Ray-trace Function

The general method of the MATLAB SuperDARN ray-trace algorithm was described in detail in the first paragraph of section 4.1.3. The flowchart of this algorithm is provided again in Figure 42 for reference. As described in section 4.1.3, the ray-trace algorithm takes inputs from the python program and traces the propagation of all rays in the list of elevations for each time, radar and beam input. For each time, the mat files containing the corresponding output SAMI data are loaded into the program. For each beam of each radar, the program uses a gridded interpolation to make a "slice" of the ionosphere along the beam for all specified ranges and altitudes. Then the raytrace2d FORTRAN function is called with the electron density grid, initial conditions and rays' elevations as inputs. Each elevation is a different ray that is traced until any of the following occur: the ray exits the ionospheric grid; the ray hits an irregularity; or the ray reaches the ground after the specified number of hops (in this case one).

The raytrace2d function outputs three structures. The two structures that are significant to our study are "ray_data" and "ray_path_data". The size of each structure is 1xNumber of Rays (Cervera 2016). The ray_data structure contains summary information for each ray including: if it reached the ground, the maximum height reached, the plasma frequency at apogee, and other information (Cervera 2016). The ray_path_data gives information on each ray at every point along its path including the ray's height, ground range and path length among other parameters (Cervera 2016). As shown in Figure 42, the ray-trace program has two outputs for each iteration: a csv file containing ray path data of all rays in a beam of a radar at one time and a mat file containing variables that are required to generate a ray-trace profile plot. As rays' path data must be loaded into python, a table containing these ray path data is generated for all rays and saved as a csv file for easy import into python. Additionally, ray_path_data and other variables are saved in a mat file for use in codes that generate ray-trace profile plots.

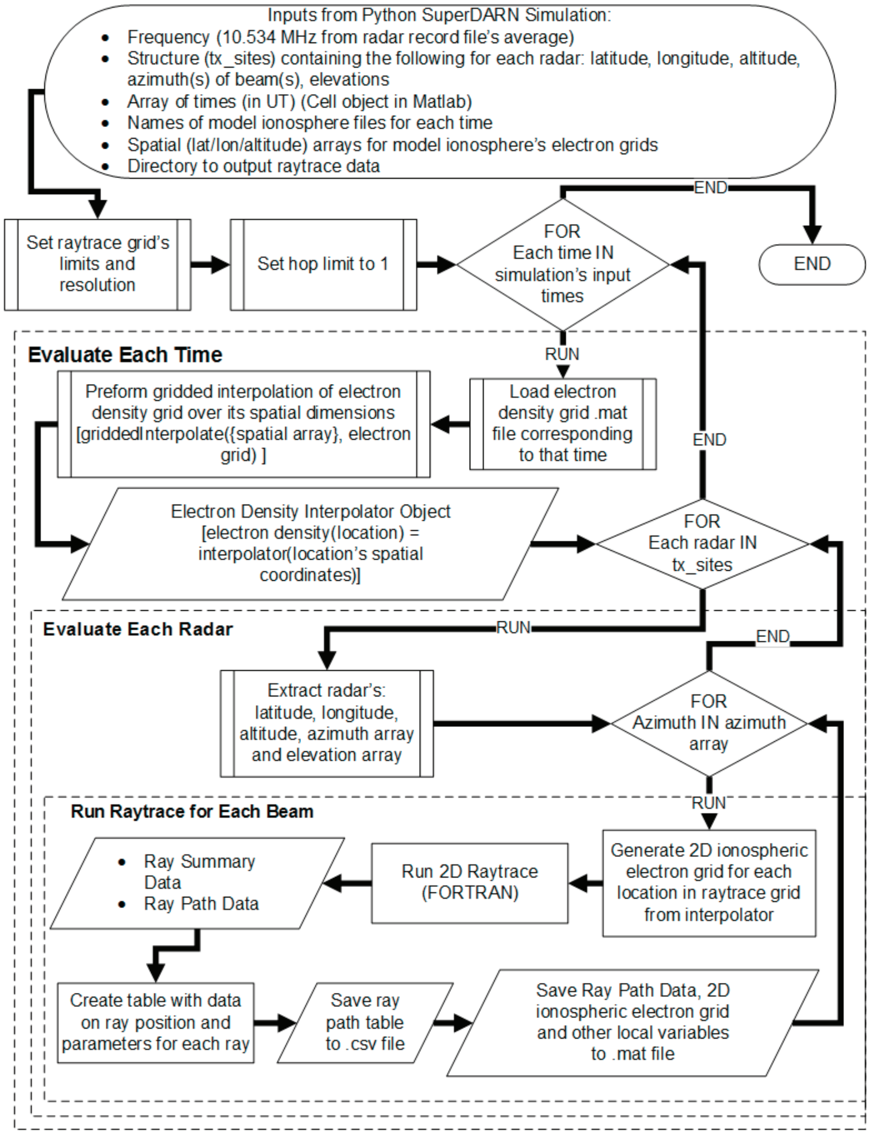

Figure 42. Flowchart of SuperDARN PHaRLAP-based ray-trace algorithm.

B.3 Python rayDarnBeamObj

The SuperDARN ray-trace simulation is orchestrated by the algorithm shown in Figure 43. This algorithm is implemented in a custom python class, called “rayDarnBeamObj”. As illustrated, the program finds the operating parameters of the input SuperDARN radar(s) and beam(s) and checks if a ray-trace has already been run the input radar(s)’ beam(s) and specified ionospheric model. If the ray-trace must be run, then the code calls the Matlab PHaRLAP wrapper with the appropriate inputs before proceeding. Then, the rayDarnBeamObj calls the custom Python class “rayDarnBeamData”. The rayDarnBeamData’s class function loads the ray-trace path data from the csv files into a data frame and then filters out any ray path data from rays that do not return to the ground before passing the data frame back to the parent rayDarnBeamObj. Finally, the data frame is passed to a function of rayDarnBeamObj that extracts the path length of each of the rays’ paths for each time as well as some other parameters that are analogous to parameters measured by SuperDARN radars (i.e. elevation angle, etc.) and bins these data into the SuperDARN radar’s range gates. Then, values in the same range gate are averaged or counted (depending on the parameter). Finally, these data are put in a dictionary of the same format as SuperDARN’s DavitPy functions use for measured data.

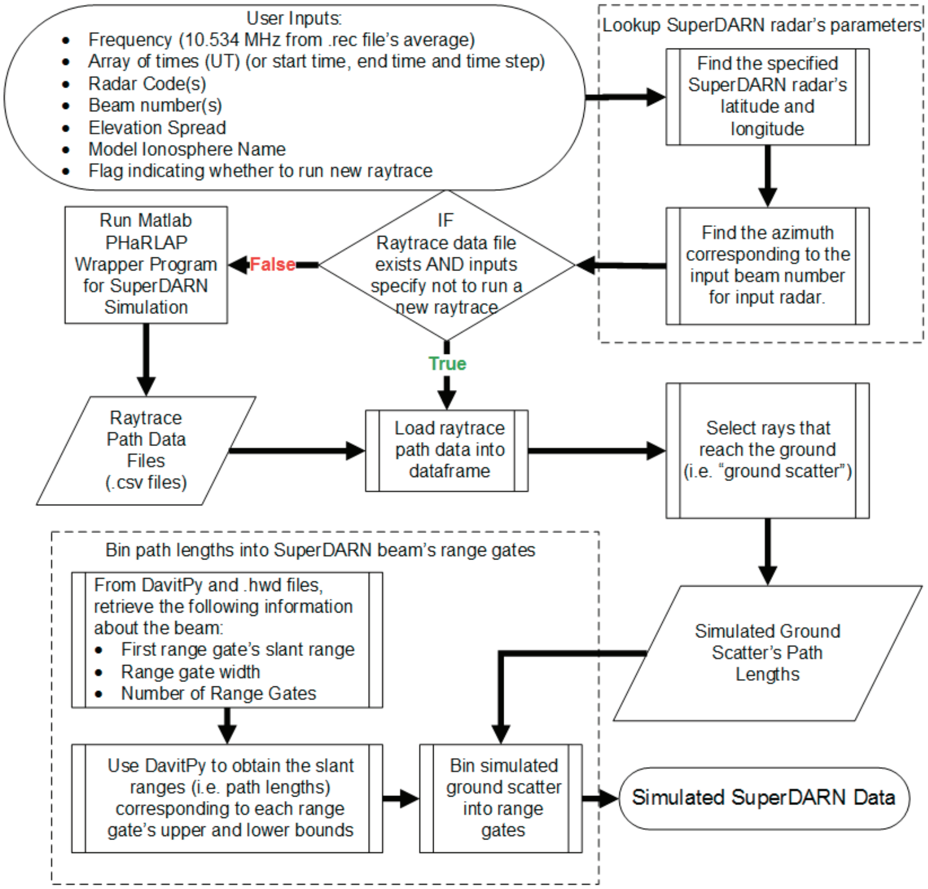

Figure 43. Flowchart of Python code that converts ray-trace path data into SuperDARN's data format.

Acknowledgements

This work was supported by NSF Grant # AGS-1552188 and NASA Grant #NNX17AH70G.

The results presented in this thesis were obtained using the HF propagation toolbox, PHaRLAP, created by Dr. Manuel Cervera, Defence Science and Technology Organisation, Australia (manuel.cervera@dsto.defence.gov.au). This toolbox is available by request from its author.

Joe Huba and Doug Drob, for SAMI3 output files used in ray-trace simulation.

We acknowledge the use of the Free Open Source Software projects used in this analysis: Ubuntu Linux, Python, iPython, matplotlib, NumPy, SciPy, scikit-learn, Davitpy, DIVA-GIS and others.

References

Afraimovich, E. L., E. A. Kosogorov and O. S. Lesyuta (2002). "Effects of the August 11, 1999 total solar eclipse as deduced from total electron content measurements at the GPS network." Journal of Atmospheric and Solar-Terrestrial Physics **64**(18): 1933-1941.

Banks, P. and G. Kockarts (1973). Aeronomy. New York, New York, Academic Press Inc.

Bowhill, S. A. (1969). Ionospheric Effects in Solar Eclipses. Solar Eclipses and the Ionosphere A NATO Advanced Studies Institute. M. Anastassiades. Lagonissi, Greece, Plenum Press.

Cervera, M. (2016). PHaRLAP. A. Defence Science and Technology Group.

Cervera, M. A. and T. J. Harris (2011). Modelling the effects of ionospheric disturbances on quasi-vertically incident ionograms using 3D magneto-ionic raytracing. 2011 XXXth URSI General Assembly and Scientific Symposium.

Chen, F. (2016). Introduction to Plasma Physics and Controlled Fusion, Springer International Publishing.

Chen, G., H. Qi, B. Ning, Z. Zhao, M. Yao, Z. Deng, T. Li, S. Huang, W. Feng, J. Wu and C. Wu (2013). "Nighttime ionospheric enhancements induced by the occurrence of an evening solar eclipse." Journal of Geophysical Research: Space Physics **118**(10): 6588-6596.

Chuo, Y. J. (2013). "Ionospheric effects on the F region during the sunrise for the annular solar eclipse over Taiwan on 21 May 2012." Ann. Geophys. **31**(11): 1891-1898.

Davies, K. (2008). Ionospheric Radio. London, United Kingdom, The Institution of Engineering and Technology.

Espenak, F. (2013 Feb 18). "GLOSSARY OF SOLAR ECLIPSE TERMS." from https://eclipse.gsfc.nasa.gov/help/SEglossary.html.

Evans, J. V. (1965). "An F region eclipse." Journal of Geophysical Research **70**(1): 131-142.

Hairston, M. R., S. Mrak, W. R. Coley, A. Burrell, B. Holt, M. Perdue, M. Depew and R. Power (2018). "Topside Ionospheric Electron Temperature Observations of the 21 August 2017 Eclipse by DMSP Spacecraft." Geophysical Research Letters **45**(15): 7242-7247.

Hargreaves, J. K. (1992). The solar-terrestrial environment. New York, NY, the Press Syndicate of the Cambridge University Press.

Huba, J. D. and D. Drob (2017). "SAMI3 prediction of the impact of the 21 August 2017 total solar eclipse on the ionosphere/plasmasphere system." Geophysical Research Letters **44**(12): 5928-5935.

Huba, J. D., G. Joyce and J. A. Fedder (2000). "Sami2 is Another Model of the Ionosphere (SAMI2): A new low-latitude ionosphere model." Journal of Geophysical Research: Space Physics **105**(A10): 23035-23053.

Huba, J. D., G. Joyce and J. Krall (2008). "Three-dimensional equatorial spread F modeling." Geophysical Research Letters **35**(10).

Jubier, X. M. (2005). "Google Earth Files (kmz)." from http://xjubier.free.fr/en/site_pages/SolarEclipsesGoogleEarth.html.

NASA. "Total Solar Eclipse of 2017 Aug 21 ", from http://eclipse.gsfc.nasa.gov/SEgoogle/SEgoogle2001/SE2017Aug21Tgoogle.html.

Nishitani, N., J. M. Ruohoniemi, M. Lester, J. B. H. Baker, A. V. Koustov, S. G. Shepherd, G. Chisham, T. Hori, E. G. Thomas, R. A. Makarevich, A. Marchaudon, P. Ponomarenko, J. A. Wild, S. E. Milan, W. A. Bristow, J. Devlin, E. Miller, R. A. Greenwald, T. Ogawa and T. Kikuchi (2019). "Review of the accomplishments of mid-latitude Super Dual Auroral Radar Network (SuperDARN) HF radars." Progress in Earth and Planetary Science **6**(1): 27.

Rishbeth, H. (1969). Theoretical Aspects of Solar Eclipses. Solar Eclipses and the Ionosphere A NATO Advanced Studies Institute. M. Anastassiades. Lagonissi, Greece, Plenum Press.

Rishbeth, H. and O. K. Garriott (1969). Introduction to Ionospheric Physics. New York; San Francisco; London, Academic Press Inc. .

Ruohoniemi, M. (2012). Remote Sensing of the Ionosphere and Earth’s Surface with HF Radar. N. F. Joseph Baker, Sebastien de Larquier, Evan Thomas Virginia Tech, Space@VT SuperDARN.

Seybold, J. S. (2005). Introduction to RF Propagation. Hoboken, NJ, John Wiley & Sons, Inc.

Sivakumar, V. (2018). Summary Of Eclipse Effects On The Ionosphere, Virginia Polytechnic Institute and State University.

Stankov, S. M., N. Bergeot, D. Berghmans, D. Bolsée, C. Bruyninx, J.-M. Chevalier, F. Clette, H. De Backer, J. De Keyser, E. D’Huys, M. Dominique, J. F. Lemaire, J. Magdalenić, C. Marqué, N. Pereira, V. Pierrard, D. Sapundjiev, D. B. Seaton, K. Stegen, R. Van der Linden, T. G. W. Verhulst and M. J. West (2017). "Multi-instrument observations of the solar eclipse on 20 March 2015 and its effects on the ionosphere over Belgium and Europe." J. Space Weather Space Clim. **7**: A19.